

**Spectral Estimation of Plasma
Fluctuations I: Comparison of Methods**

**Kurt S. Riedel and Alexander Sidorenko,
Courant Institute of Mathematical Sciences
New York University
New York, New York 10012-1185**

**David J. Thomson
AT&T Bell Laboratories
Murray Hill, NJ 07974-0636**

Abstract

The relative root mean squared errors (RMSE) of nonparametric methods for spectral estimation is compared for microwave scattering data of plasma fluctuations. These methods reduce the variance of the periodogram estimate by averaging the spectrum over a frequency bandwidth. As the bandwidth increases, the variance decreases, but the bias error increases. The plasma spectra vary by over four orders of magnitude, and therefore, using a spectral window is necessary. We compare the smoothed tapered periodogram with the adaptive multiple taper methods and hybrid methods. We find that a hybrid method, which uses four orthogonal tapers and then applies a kernel smoother, performs best. For 300 point data segments, even an optimized smoothed tapered periodogram has a 24 % larger relative RMSE than the hybrid method. We present two new adaptive multitaper weightings which outperform Thomson's original adaptive weighting.

PACS 52.35, 52.55, 52.70, 06., 2.50

I. Introduction

The measurement and analysis of plasma fluctuations have become increasingly important as the magnetic fusion community attempts to understand and cure plasma turbulence. Two excellent reviews summarize the experimental work on plasma fluctuations and anomalous tokamak transport.^{1–2} To understand the precise nature of the drift wave turbulence, we hope to determine the experimental dispersion relation, the rollover points, ω_R , of the fluctuation spectrum (the value of ω and \vec{k} where the fluctuations are the largest), and the spectral decay exponents.

In this article, our goal is to more efficiently and accurately determine the spectral distribution of plasma fluctuations for a given length digitalized time series. We compare a number of different methods^{3–10} to estimate the spectral density of fluctuations using actual fusion data. We concentrate on time stationary fluctuations. In a successor article, we present a number of applications of multitaper spectral analysis^{3–7} to nonstationary times series^{11,12}.

We analyze time series data from the Tokamak Fusion Test Reactor¹³ (TFTR) microwave scattering diagnostic^{14–17}. Because the TFTR spectrum varies over four orders of magnitude, the standard techniques^{8–10} of spectral analysis do not necessarily perform well. Therefore, we compare the estimation methods on data which is typical of forward scattering experiments. All of the spectral estimation methods in our study yield nearly identical estimates for the entire 45,000 point data segment of interest. When the plasma fluctuations are nonstationary, much shorter time segments must be used. Therefore, we compare the relative accuracy of several spectral estimations methods on data segments of 300-3000 points. *For these short sample lengths, we show that the advanced analysis techniques significantly outperform the conventional estimates.*

All of the methods essentially average over some frequency bandwidth to reduce the variance. As the bandwidth is increased, more degrees of freedom are used. If the bandwidth is too large, the spectral estimate will be artificially broadened, and a bias error will result. Thus selecting the “correct” bandwidth is crucial, and we choose the optimal global bandwidth for each method separately.

In Section II, we describe the physics of the TFTR microwave scattering experiment. In Section III, we review the standard approach to estimating spectral densities. In Section IV, we describe and apply a family of advanced statistical techniques for estimating spectral densities: multitaper spectral methods^{3–7}. Multiple taper methods have been successfully applied to a number of different problems in geophysics. Sections III and IV present some of the results of the comparison described in Sec. VI. In Section V and Appendix C, we describe the jackknife procedure^{18–20} for non-

parametric variance estimation.

In Section VI, we compare the accuracy of the various spectral estimation techniques using the TFTR data. We examine the relative accuracy of the smoothed periodogram and the multiple taper analysis for 300–3000 point data subsegments. We show that both methods yield the nearly identical estimates for long data segments and that multitaper converges more rapidly. Unexpectedly, we find that *a hybrid method where the multitaper spectral estimate is then smoothed performs appreciably better* than either the smoothed periodogram or the “pure” multitaper. We summarize our results on the estimation of TFTR spectra in Sec. VII. In Appendix A, we summarize the properties of the Slepian tapers²¹ which form the bases for multitaper analysis. In Appendix B, we present two new adaptive weightings for multitaper estimation: sequential deselection and the minimal expected loss weighting. Appendix D gives the details of our empirical RMSE comparison.

II. TFTR microwave scattering dataset

We now describe the TFTR data and the physics of the underlying fluctuations. The microwave transmitter launches a 60 GHz plasma wave linearly polarized in the extraordinary mode below the electron cyclotron frequency^{14,15}. The 112 GHz extraordinary mode plasma wave propagates from the top of the plasma to the core plasma, where the plasma density fluctuations scatter the incoming wave^{22–25}. The scattered wave is measured by a receiver located near the bottom of the vacuum vessel so that $|\vec{k}_{scat} - \vec{k}_{inc}| \simeq 3$ cm and \vec{k} is parallel to the poloidal magnetic field at $\frac{r}{a} \simeq .3$. The scattered signal is proportional to the density fluctuations.

The plasma waves are believed to consist of an ensemble of drift waves^{1,2,25}. For electron drift waves, the characteristic frequency is the electron drift frequency $\omega \sim \omega_{D_e} \equiv dn_e/dr$ and the characteristic distance is $\rho_S \simeq \rho_i \sqrt{T_e/T_i}$, where ρ_i is the ion-cyclotron radius. Since the drift waves are localized near the Doppler-shifted resonance surface, the drift wave dispersion relation is approximately $\omega \sim V_{D_e} k_\theta$. Including the zeroth order Larmor radius effects modifies the dispersion relation to $\omega \sim v_{D_e} k_\perp / (1 + k_\perp^2 \rho_S^2)$, where $v_{D_e} \equiv \frac{T_e}{eB} \frac{d \ln(n_e)}{dr}$. From mixing length theory, we expect the saturated fluctuation amplitudes to be approximately

$$\frac{\delta n}{n} \sim \frac{e \delta \Phi}{\kappa T_e} \sim \frac{1}{k_\perp L_n},$$

where L_n is the equilibrium density gradient scale length.

For TFTR discharge number 50616, the plasma parameters are $B_t = 4$ Tesla, $I_p = 1.2$ MA, $\bar{n} = 3.6 \times 10^{15}$ cm⁻³. The central electron temperature is approximately

2 Kev and the central ion temperature is approximately 1 Kev. In the scattering volume, the local plasma parameters are $\rho_i = 0.08$ cm, $\rho_S = 0.11$ cm, $k_\theta \simeq 3$ cm⁻¹, $V_{DE} = 4.9 \times 10^4$ m/sec, $\omega_{De}/2\pi = 23$ kHz.

In most drift wave theories, both short and long wavelength drift waves are stable, and only moderate wave length drift waves are unstable. We expect the largest amplitude fluctuations to occur at $k\rho_S \sim .1 - .5$. Typically, $\omega_{measured} \simeq (2 - 4)\omega_e^*$, possibly due to toroidal plasma rotation.

The time series begins 5.0 sec. into the discharge, and is totally contained in the Ohmic phase. We redefine time equals zero ($t \equiv 0$) as the start of our series. A macroscopic sawtooth oscillation occurs at 3.86 millisec into the dataset. During this time, the plasma is strongly nonstationary and the analysis requires the methods of our successor article¹¹. The scattering volume lies just outside the sawtooth mixing radius.

Our data consists of 65,500 time samples with a uniform sampling rate 5 MHz over the time interval. Thus the fluctuations are recorded over a tenth of a second time interval. The data has been low-pass filtered with an anti-aliasing filter with a filter halfwidth of 2.5 MHz. The spectral peak at 1 MHz corresponds to the receiver intermediate frequency (IF), and is caused by wall and waveguide reflections. The broadening of the 1 MHz peak is believed to be due to intense edge fluctuations^{16,17}.

In this article, we concentrate on obtaining the best possible estimates of the fluctuation spectrum during the stationary part of the discharge. Thus we consider only the 45,000 datapoints beginning .24 millisec after the sawtooth.

III. Single Taper Spectral Analysis

A. INTEGRAL FORMULATION OF STATIONARY PROCESSES

We consider a stationary stochastic process with no deterministic spectral lines. We are given N discrete measurements, $\{x_{-\lfloor \frac{N}{2} \rfloor}, \dots, x_0, x_1, \dots, x_{\lfloor \frac{N}{2} \rfloor}\}$, of a realization of the stochastic process. For convenience, we assume that the data length is an odd integer, and define $\lfloor \frac{N}{2} \rfloor \equiv (\frac{N-1}{2})$. We index the data such that the midpoint of the data is measured at time equal to zero. The Nyquist frequency is $\frac{1}{2\Delta t}$, and the Rayleigh resolution frequency is $\frac{1}{N\Delta t}$. We define the time-frequency bandwidth, $\bar{W} \equiv WN\Delta t$, where W is the frequency bandwidth. We normalize the time interval, Δt , between measurements to unity.

The Cramer representation of a stationary stochastic process^{8–10} is

$$x_n = \int_{-1/2}^{1/2} e^{2\pi i f n} dZ(f) , \quad (1)$$

where dZ is a random measure. Stationarity implies that dZ has independent spectral increments, i.e. the values of dZ at different frequencies, f and g , are uncorrelated. We assume that the spectral measure is absolutely continuous with a spectral density $S(f)$. Thus the covariance of dZ satisfies

$$\mathbf{E}[dZ(f)d\bar{Z}(g)] = S(f)\delta(f-g)dfdg. \quad (2)$$

The measured time series, $\{x_i\}$, has a discrete Fourier transform, $y(f)$:

$$y(f) = \sum_{n=-\lfloor \frac{N}{2} \rfloor}^{\lfloor \frac{N}{2} \rfloor} x_n e^{-2\pi i n f} , \quad (3)$$

and a corresponding inverse:

$$x_n = \int_{-1/2}^{1/2} y(f) e^{+2\pi i n f} df . \quad (4)$$

Substituting Eq. (1), we obtain the Cramer representation of the discrete Fourier transform,

$$y(f) = \int_{-1/2}^{1/2} \sum_{n=-\lfloor \frac{N}{2} \rfloor}^{\lfloor \frac{N}{2} \rfloor} e^{-2\pi i n(f-f')} dZ(f') = \int_{-1/2}^{1/2} \frac{\sin(N\pi(f-f'))}{\sin(\pi(f-f'))} dZ(f') . \quad (5)$$

Thus the discrete Fourier transform of the measured process is related to the realization of the stochastic process by an integral equation of the first kind. Similarly,

the expectation of the discrete periodogram, $I(f) \equiv |y(f)|^2$, is related to the spectral distribution, $S(f)$, via a convolution equation with the Fejér kernel:

$$\mathbf{E}[I(f)] \equiv \mathbf{E}[|y(f)|^2] = \frac{1}{N} \int_{-1/2}^{1/2} \left[\frac{\sin(N\pi(f-f'))}{\sin(\pi(f-f'))} \right]^2 S(f') df'. \quad (6)$$

We note that *Eq. (5) applies to the particular realization of the stochastic process, $dZ(f)$, which has been observed, and that Eq. (6) applies to the expectation of the periodogram.* In the next subsection, we show that the standard deviation of the simple periodogram estimate, $|y(f)|^2$, is approximately equal to the spectrum itself^{8–10}. *Thus the variance of the periodogram estimate is large, and does not converge with N .*

To estimate the bias of the simple periodogram estimate of the spectrum, we make a Taylor series expansion of $S(f)$ about f : $S(f + \tilde{f}) \sim S(f) + S'(f)\tilde{f} + S''(f)\tilde{f}^2/2$ and substitute the expansion into Eq. (6):

$$\mathbf{E}[I(f)] \sim S(f) + \frac{S''(f)}{2} \int_{-1/2}^{1/2} \frac{(f-f')^2}{N} \left[\frac{\sin(N\pi(f-f'))}{\sin(\pi(f-f'))} \right]^2 df'. \quad (7)$$

The standard approach to reducing the bias of spectral estimate is to apply a data taper, and thereby reduce the sidelobes of the kernel.

B. BRIEF OVERVIEW OF SPECTRAL ESTIMATION

The inverse spectral problem is to determine $S(f)$, given the time series data: $\{x_{-\lfloor \frac{N}{2} \rfloor}, \dots, x_0, x_1, \dots, x_{\lfloor \frac{N}{2} \rfloor}\}$. The inverse problem can be viewed as a coupled set of integral equations: Eq. (5) relates $y(f)$ to the random process, $dZ(f)$, and Eq. (6) relates $E|y(f)|^2$ to the spectral density $S(f)$.

Our basic goal is to invert the Fejér integral equation, Eq. (6), to determine $S(f)$. Equation (6) is an integral equation of the first type. The standard numerical method for the inversion of integral equations of the first kind is to regularize the equation by adding a small smoothness penalty function of the form $\int [S''(f)]^2 df$. Spectral estimation contains essentially three difficulties which require more specialized techniques.

First, the values of the estimated periodogram, $I(f)$, are correlated in the frequency domain, and therefore, the estimation technique needs to take account of this correlation to be effective.

Second, most numerical inversion techniques produce broader and smoother spectral estimates than the true spectra. This bias is especially disadvantageous when the

spectrum has one or more narrow peaks and the shape of the spectrum is of primary interest. In turbulent plasma fluctuations, the exponent of the spectral rolloff helps to determine the nature of the turbulent fluctuations.

Third, Eq. (6) assumes the spectrum is purely incoherent and uses only the amplitude of $y(f)$. Thus the phase information in $y(f)$ is ignored. When the spectrum contains coherent components such as spectral lines, the phase information is crucial in estimating the coherent component. Therefore, we attempt to invert Eq. (5), and determine the realization of $dZ(f)$ before estimating $S(f)$.

C. BIAS AND VARIANCE OF SINGLE TAPER ESTIMATES

The standard single taper theory of nonparametric spectral analysis^{8–10} multiplies the data by a taper, ν_n , $n = -[\frac{N}{2}], \dots, [\frac{N}{2}]$, prior to performing the Fourier transform, in order to reduce the bias from the sidelobes of the Fejér kernel. Thus the tapered transform is

$$y_\nu(f) = \sum_{n=-[\frac{N}{2}]}^{[\frac{N}{2}]} x_n \nu_n e^{-2\pi i n f} . \quad (8)$$

We define the spectral window, $V(f)$, to be the Fourier transform of ν_n :

$$V(f) = \sum_{n=-[\frac{N}{2}]}^{[\frac{N}{2}]} \nu_n e^{-2\pi i n f} , \quad \nu_n = \int_{-1/2}^{1/2} V(f) e^{2\pi i n f} df . \quad (9)$$

To reduce the bias from spectral leakage, the taper should be localized in the frequency domain. The expectation of the second moment of the tapered estimator is

$$\mathbf{E}[(y_\nu(f_1)y_\nu^*(f_2))] = \int_{-1/2}^{1/2} V(f - f_1)V^*(f - f_2)S(f)df . \quad (10)$$

We decompose the bias of the tapered spectral estimate into the narrow banded part from $|f' - f| < W$, and the broad-banded part. For a taper to be useful in reducing the broad-banded bias, the sidelobes of $|V(f' - f)|^2$ should decay faster than $\left[\frac{\sin(N\pi(f-f'))}{\sin(\pi(f-f'))}\right]^2$. Figure 1 plots the tapered and untapered kernels for $N = 100$, where $V(f)$ is the Slepian spectral window²¹ which is described in Appendix A. For $N \geq 100$, the sidelobes of both kernels are small on the linear scale. If the spectrum varies rapidly on the logarithmic scale, these sidelobes can cause considerable bias. Figure 2 displays the kernels on the logarithmic scale for $N = 300$. Both the Fejér kernel and the tapered kernel decay as f^{-2} , but the amplitude of the tapered sidelobes is reduced proportionally to $\exp(-NW)$ relative to the Fejér kernel.

A third family of tapers which we use is the Tukey α split cosine taper where

$$\begin{aligned}\nu_j &= \frac{1}{2}[1 - \cos(\frac{\pi(j-1/2)}{\alpha N})] && \text{for } 1 \leq j < \alpha N ; \\ \nu_j &= 1 && \text{for } \alpha N \leq j \leq (1 - \alpha)N ; \\ \nu_j &= \frac{1}{2}[1 - \cos(\frac{\pi(N-j+1/2)}{\alpha N})] && \text{for } (1 - \alpha)N < j \leq N .\end{aligned}$$

The α parameter determines the extent of the tapering. As α increases, the bias protection improves at the cost of discarding more data. Traditionally, α is set at .1, but recently Hurvich has shown that αN should be approximately constant as N increases²⁶. Our RMSE comparison supports Hurvich's conclusion, and we find that $\alpha N \sim 30\text{--}50$ works best for 300-3000 point segments of the TFTR data.

We now restrict our consideration to *Gaussian stationary processes*. In this case, the covariance of the quadratic tapered estimator is

$$\begin{aligned}\mathbf{Cov} [|y_\nu(f_1)|^2, |y_\nu(f_2)|^2] = \\ \left| \int_{-1/2}^{1/2} V(f - f_1) \bar{V}(f - f_2) S(f) df \right|^2 + \left| \int_{-1/2}^{1/2} V(f - f_1) \bar{V}(f + f_2) S(f) df \right|^2 .\end{aligned}\quad (11)$$

When V is localized about zero, the second term is only important when both f_1 and f_2 are within a bandwidth of zero frequency or the Nyquist frequency. We will usually neglect this second term. Generally, the Gaussian assumption is reasonable to estimate $\mathbf{Cov} [|y_\nu(f_1)|^2, |y_\nu(f_2)|^2]$ when $S(f)$ is smooth, but higher moments will be increasingly sensitive to the Gaussian assumption. In Sec. V, we compare the Gaussian error bars with a nonparametric estimate. We find that the Gaussian error bars actually overestimate the variance, probably due to the coherent component of the signal.

We note that $|y_\nu(f)|^2$ is approximately distributed as a χ_2^2 distribution, and therefore has a variance almost exactly equal to the square of its expectation. *Thus the quadratic taper estimate for the spectral density is inconsistent, i.e. the variance of the estimate is fixed, and does not tend to zero as the number of data points, N , increases.*

Figure 3 plots the untapered periodogram estimate of the spectral density for the entire 45,000 point data segment. The rapid oscillation is characteristic of the χ_2^2 distribution of $|y(f)|^2$.

When we use the entire 45,000 points of data, the bias of the periodogram is small over much of the frequency range. For nonstationary phenomena, a more typical data length is several hundred data points. Therefore, we examine the estimated spectrum for a typical 300 point data segment corresponding to a time interval of .06 millisecc. Figure 4 plots the periodogram spectral estimate for the 300 point

subsegment beginning at time = 8.6 millise. The spectrum is appreciably broader than the 45,000 point estimate of Figs. 3 & 5 due to the coarse resolution $\sim \frac{1}{300\Delta t} = 17\text{kHz}$. The coherence frequency scalelength for the random fluctuations to occur in the periodogram is also $\sim \frac{1}{300\Delta t}$. *To reduce the variance of the spectral estimate, most statistical methods average over a frequency interval or over time segments.*

D. CONSISTENT SPECTRAL ESTIMATORS: THE SMOOTHED PERIOGRAM

The point tapered spectral estimate, $\hat{S}_\nu(f) = |y_\nu(f)|^2$, has an approximately χ^2_2 distribution, and therefore a variance of $\mathbf{E}[\hat{S}_\nu]^2$ to leading order. Thus this raw spectral estimate is statistically inconsistent in the sense that $\hat{S}_\nu(f)$ does not tend asymptotically to $S(f)$ as the time series length increases. There are two standard remedies.

First, if a number, N_s , of independent, statistically identical time series are available, the spectral estimates from the individual series may be averaged to produce a mean estimate: $\bar{S} \equiv \frac{1}{N_s} \sum_{k=1}^{N_s} \hat{S}_k(f)$. The mean estimate, \bar{S} , has a variance approximately equal to $S(f)^2/N_s$.

Second, for a single time series, statistical consistency is normally achieved by smoothing the raw spectral estimate over a bandwidth, W . This kernel smoothing decreases the variance of the spectral estimate while increasing the bias. The theory of optimal kernel smoothing is quite advanced^{27,28}. For our analysis, *we use a simple boxcar average with a fixed kernel halfwidth.*

The solid line in Fig. 5 plots the smoothed periodogram for the entire data segment with a kernel halfwidth of 14 kHz. The central peak at 1 MHz is partially coherent and is believed to be due to reflection from the waveguide and vacuum vessel wall, broadened by fluctuations at the plasma edge^{16,17}. *The secondary peak at 550 kHz is generated by fluctuations with phase velocities in the electron drift direction.* These fluctuations have a frequency spread of ± 100 kHz. The dashed line gives the smoothed tapered estimate using the same kernel halfwidth of 14 kHz. We use a Tukey split cosine taper with $\alpha N = 100$. Thus we trim only 200 data points out of 45,000. Nevertheless, a slight difference in the curves is visible at the highest frequencies. The dotted curve is the multitaper estimate, and will be discussed in the next section.

The dashed line in Fig. 4 is the periodogram with $W = 70$ kHz. By smoothing, we have reduced the variance at the cost of less frequency resolution. The dotted curve is the smoothed tapered estimate using $W = 70$ kHz and the Tukey split cosine taper with $\alpha N = 33$. For $|f| > 1.6$ MHz, the smoothed periodogram is larger than the corresponding tapered curve. Without tapering, the spectral estimates with small

values of $S(f)$ are artificially increased due to bias towards broadening due to the $\left[\frac{\sin(N\pi f)}{\sin(\pi f)}\right]^2$ kernel in Eq. (6).

Figure 6 plots the smoothed tapered periodogram for the 300 point subsegment of Fig. 4 for three different kernel halfwidths, 40 kHz, 70 kHz, 120 kHz. As the kernel halfwidth increases, the spectrum is smoothed and artificially broadened.

Figure 7 plots the relative RMSE of the three different kernel halfwidths, averaged over 299 different subsegments. The calculation of the RMSE is described in Sec. VI and Appendix D. The RMSE increases with increasing bandwidth near the spectral peaks. For larger frequencies, the spectral variation is less and the optimal bandwidth is greater than 120kHz. Thus an improved estimation procedure would be to use a small bandwidth near the peaks and a larger bandwidth for the flatter parts of the spectrum.

IV. Multiple Taper Spectral Analysis

Multiple taper spectral estimation was presented in Ref. 3, developed in Refs. 4-7, and has been used with good success in geophysical applications. Thomson's theory treats spectral analysis as an inverse problem for the integral equation of the first kind given in Eq. (5). We solve the integral equation by expanding in a set of eigenfunctions of a similar integral equation with a band-limited kernel.

As an alternative to the smoothed kernel estimate, Thomson³ proposed to use a family of the orthogonal Slepian tapers²¹, $\{\nu_i^{(0)}\}, \{\nu_i^{(1)}\}, \dots, \{\nu_i^{(K-1)}\}$, where $K \equiv 2NW$. Appendix A describes the family of tapers which we use for both the single and multiple taper analysis. The bandwidth, W , is a free parameter for the Slepian tapers. To begin the multitaper spectral analysis, we estimate each of the K tapered transforms:

$$y^{(k)}(f) = \sum_{n=-\lfloor \frac{N}{2} \rfloor}^{\lfloor \frac{N}{2} \rfloor} x_n \nu_n^{(k)} e^{-2\pi i n f} . \quad (12)$$

In the frequency domain, this corresponds to the convolution equation:

$$\hat{y}_\nu^{(k)}(f_1) = \int_{-1/2}^{1/2} V^{(k)}(f - f_1) y(f) df = \int_{-1/2}^{1/2} V^{(k)}(f - f_1) dZ(f) . \quad (13)$$

The different tapered estimates, $|y^{(k)}(f)|^2$, are statistically independent to $O\left(\left|\frac{WS'(f)}{S(f)}\right|^2\right)$. Thus we have effectively created $2NW$ independent realizations of a band-limited stochastic processes.

We then construct the K raw estimates of the spectral density: $\hat{S}_k(f) = |y^{(k)}|^2$, which are combined to produce a “simple” multitaper spectral estimate:

$$\bar{\hat{S}} \equiv \frac{1}{K} \sum_{k=0}^{K-1} \hat{S}^{(k)}(f) . \quad (14)$$

In multiple taper estimation, each of *the estimates*, $y^{(k)}(f)$, *is not only independent, but also centered at the frequency f* . In contrast, smoothed single taper estimates are averages of $y_\nu(f + f')$ as f' varies, and $y_\nu(f + f')$ is centered about the frequency $f + f'$, not f . As a result, multiple taper analysis is more efficient, and has a lower bias than the smoothed tapered periodogram.

Each of the eigentaper estimates, $\hat{S}_k(f)$, has a slightly different bias and variance, and therefore, the spectral estimate can be improved by replacing the simple average of the $\hat{S}^{(k)}$ with a weighted linear combination of these estimates:

$$\hat{S}_c(f) \equiv \sum_{k=0}^{K-1} c_k(f) \hat{S}^{(k)}(f) , \quad (15)$$

where $c_k(f)$ are weights. The adaptive weightings differ from a uniform weighting, $c_k \equiv \frac{1}{K}$, by terms of $O(S''(f_1)W^2)$ and of $O(1 - \lambda_k)$. Appendix B presents three different adaptive weightings. In this section, we use the *sequential deselection adaptive weighting*. The main effect of the adaptive weightings is to downweight the last tapers, ($k = K, K - 1$), when $\sigma^2(1 - \lambda_k) \gg S(f)$.

The multitaper estimate of the entire data segment with the sequential deselection adaptive weighting is given as the solid curve of Fig. 5. We have used 252 tapers corresponding to a bandwidth of 14 kHz. The spectral decay appears exponential over four decades and not algebraic. The adaptive multitaper estimate and the smoothed tapered periodogram are virtually identical, showing that the difference in the estimates tends to zero as N increases.

Increasing the bandwidth and the corresponding number of tapers decreases the variance and raises the smoothing bias. Figure 8 compares the estimated spectrum for different values of W . The spectral estimates in Figs. 6 & 8 are similar and show that choosing the correct bandwidth is the most important aspect of spectral estimation. The effective bandwidth of the smoothed tapered periodogram is larger due to the finite support of the Fejér kernel. Therefore, the optimal bandwidth of multitaper analysis is larger than that of the smoothed tapered periodogram.

To compare the adaptive weighting of Eq. (15) with the uniform weighting multitaper estimate of Eq. (14), we compute both estimates on 300 point subsegments. (We average over 299 different subsegments to reduce the variance of the estimate and

thereby emphasize the effect of the bias error.) Figure 9 plots the averages of the two estimates. Near 1 MHz, the two weightings are identical, while for $f > 1.5\text{MHz}$, the nonadaptive weighting oscillates with a frequency of $\frac{1}{N\Delta t}$. The dashed line gives the uniform weighting multitaper estimate with the same bandwidth, but without using the last two tapers, $k = K - 1, K$. The artificial oscillation is noticeably smaller, indicating that the last tapers are primarily responsible. The variance of this estimate near 1 MHz is larger due to the absence of the last tapers. The adaptive multitaper estimate uses the maximum number of tapers when the spectrum is large while effectively eliminating the most biased tapers when the spectral density is much smaller than the average density.

In Sec. VI, we also consider “*hybrid*” methods where the multitaper estimate is then kernel smoothed. The total bandwidth is the multitaper bandwidth plus the kernel smoother width. Hybrid methods offer the possibility of using essentially all of the degrees of freedom in the frequency bandwidth (like multitaper) with the flexibility and data adaptivity of a *variable* halfwidth kernel smoother²⁸.

V. Jackknife Estimates of Bias and Variance of Multiple Taper Spectra

We now examine estimates of the variance of our multiple taper spectral estimate⁴. Appendix C is a short review of the jackknife resampling technique. The most straightforward estimate of the variance of the multitaper spectral estimate is

$$\hat{\sigma}^2(f) = \frac{1}{K(K-1)} \sum_{k=0}^{K-1} \left[\hat{S}^{(k)}(f) - \bar{\hat{S}}(f) \right]^2, \quad (16)$$

where $\bar{\hat{S}}(f)$ is the simple arithmetic mean of the multiple taper spectral estimate. Eq. (16) is adequate to estimate the variance of $\bar{\hat{S}}(f)$. However, it tends to underestimate the probability of tail events when the distribution is non-Gaussian, and it does not generalize easily to the nonlinear adaptive weightings.

To robustify the variance estimate against non-Gaussian, large tail effects, we transform to the logarithmic scale. To estimate $\ln(S)$, we use the logarithm of the mean:

$$\ln[\widehat{\bar{S}}(f)] \equiv \ln \left(\frac{1}{K} \sum_{k=0}^{K-1} \hat{S}^{(k)}(f) \right), \quad (17)$$

instead of the mean of the logarithms:

$$\overline{\ln[\hat{S}(f)]} \equiv \frac{1}{K} \sum_{k=0}^{K-1} \ln(\hat{S}^{(k)}(f)). \quad (18)$$

Appendix C shows that Eq. (18) has both larger bias and variance than Eq. (17). A related advantage of the logarithmic transformation is that $\widehat{\ln S}(f)$ converges in distribution more rapidly to a Gaussian than does $\hat{S}(f)$. Thus the confidence intervals for the transformed variable are more accurate.

Equation (18) is biased downward, and the confidence intervals for $\widehat{\ln S}(f)$ are still based on the Gaussian assumption. To correct for the downward bias and to remove the Gaussian assumption, we use the resampling technique of jackknifing. In accordance with Appendix C, we use the delete-one samples to compute the variance as given by Eq.(C?). The jackknife further reduces the effects of the large tail in the probability distribution, and thereby aids in the convergence of our estimate in the variance of the combined estimate of $\ln(S(f))$. The jackknife also allows us to propagate the effects of the nonlinear adaptive weightings into the error analysis.

Figure 10 depicts the jackknife estimate of 2σ confidence interval for $S(f)$. The dotted line gives the corresponding error estimates for *Gaussian* processes. The Gaussian error bars are actually larger than the empirical error bars near the spectral peaks. This unusual result occurs because the spectral peaks are partially coherent i.e. contain a small number of waves which are oscillating in phase. In contrast, the Gaussian error bar assumes not only that the process is Gaussian, but also that it is zero mean (no coherent component), and it is this assumption that probably breaks down.

VI. Empirical Comparison of Spectral Estimation Methods

We have described the theoretical advantages of multitaper and smoothed multitaper analysis over the smoothed periodogram. The extent of the advantages is a function of the unknown spectrum and the sampling rate. We now make a detailed study of the performance advantages of multitaper analysis over conventional methods for the TFTR fluctuations with 300-3000 point samples. Because the spectral range of the TFTR dataset is more than four orders of magnitude, we make our comparison on the logarithmic scale. We compute the estimated spectrum and the inferred RMSE for the various methods on 299 subsegments of length 300 with 50 % overlap. Because the true spectrum is unknown, we use the 45,000 point estimates in Fig. 5. The technical details of the comparison are given in Appendix D.

Figure 6 gives the relative RMSE, normalized to the converged spectrum, of the smoothed periodogram for different bandwidths. Clearly, the “best” bandwidth is a function of frequency. To determine which bandwidth is optimal globally, we need to specify how we wish to weight the RMSE as a function of frequency. We note that

the errors are much larger at the spectral peaks. A simple averaging of the RMSE or even the relative RMSE will be dominated by the fit to the spectral peaks. Instead, we concentrate on an accurate estimate of the spectral density away from the peaks. Thus we consider the relative RMSE averaged over the frequency bands, $[200, 900]$ kHz, $[1100, 1900]$ kHz, and $[2100, 2400]$ kHz.

The different methods have different effective bandwidths for the same “official” bandwidth, due to the finite support of the kernel in Eq. (10). For each method separately, we determine the optimal bandwidth by minimizing the relative RMSE averaged over the combined frequency bands, $[200, 900]$ kHz plus $[1100, 1900]$ kHz plus $[2100, 2400]$ kHz. Table 1 gives the integrated relative RMSE for each estimate. Table 2 gives the kernel halfwidth which minimizes the integrated relative RMSE for each method.

We begin by comparing the dependence of the relative RMSE on the taper shape. We then compare the three different adaptive weightings of Appendix B. Finally, we conclude by comparing the hybrid, smoothed multitaper with the best adaptive multitaper estimate and the best smoothed tapered periodogram.

A. COMPARISON OF TAPERS FOR THE SMOOTHED PERIODOGRAM

We compare the Tukey split cosine taper and the Slepian taper with no tapering for the smoothed periodogram. Both the Tukey split cosine taper and the Slepian taper have auxiliary parameters, α for the Tukey split cosine taper and \bar{W} for the Slepian taper. In both cases, we optimize the taper parameter with respect to the integrated relative RMSE. We find that the best αN for the Tukey taper grows very slowly with N (See Table 2). The integrated relative RMSE is a weak function of αN .

Figure 11 plots the relative RMSE for each taper. The untapered periodogram performs so poorly that its relative RMSE is 2.5 times the RMSE of the Tukey taper at high frequencies. For $|f| > 2.1$ MHz, the bias error is most pronounced and the periodogram’s RMSE is *four* times that of the tapered smoothed periodogram is used. As N increases, the dominating effect of nonlocal bias on the smoothed periodogram decreases.

For $N = 300$, the Tukey taper outperforms the Slepian taper at high frequencies, and the Slepian taper does better at the spectral peaks. Since the Slepian taper windows more of the data than does the Tukey taper, the Slepian taper offers more protection against broad-banded bias at the cost of having a larger variance. For $N = 1000$, the Slepian taper loses much of its advantage near the peaks, while continuing to have higher variance than the Tukey taper. As N increases, the broad-banded

bias protection is less necessary. By fixing $\alpha N \sim \text{constant}$, a decreasing percentage of the data is tapered²⁶. In contrast, the Slepian taper cannot be relaxed towards no tapering and continues to taper a fixed percentage of the data even when such strong bias protection is unnecessary. Multitaper analysis circumvents this problem by using additional tapers.

B. COMPARISON OF ADAPTIVE WEIGHTINGS FOR MULTITAPER ESTIMATION

Figure 12 plots the normalized RMSE for each of the three adaptive weightings of the multitaper estimate plus the unweighted estimate for $N = 300$. *Sequential deselection performs best, followed by the minimal loss weighting.* For $N = 300$, the sequential deselection estimate has an average relative error of 40 %, which is appreciable. Table 1 shows that our new adaptive weightings can reduce the error by 15 % relative to the error of the Thomson’s adaptive weighting³ (Eq. (B6)) and by 25 % relative to the unweighted estimate.

We have examined the contributions of the bias and variance to the total RMSE. Thomson’s weighting has the lowest value of the bias. Our new weightings, sequential deselection and minimal loss, deliberately bias the estimate downward to reduce the expected error (by using the denominator $\frac{1}{K+1}$ instead of $\frac{1}{K}$). The minimal loss weighting has an additional weighting factor, $\left(\lambda_k + \frac{\sigma^2}{S(f)}(1 - \lambda_k)\right)^{-1}$, which is intended to correct the estimates for broad-banded bias. Unfortunately, our study finds that this correction almost always has a larger bias error than does sequential deselection. Presumably, the bias correction fails because the actual spectrum differs significantly for the spectrum assumed in the model weighting. (See the second from the last paragraph in Appendix B.)

When N increases, the advantage of sequential deselection over previous multitaper methods is reduced somewhat, but is still noticeable. All four weightings produce similar estimates for $|f| < 1.5$ MHz, however as the spectrum decreases and the bias increases, the adaptive weightings have noticeable differences.

C. MULTITAPER – SMOOTHED MULTITAPER – SMOOTHED PERIODOGRAM COMPARISON

Our final and most important result is that *the smoothed multitaper estimate outperforms the best “pure” multitaper and the best “pure” smoothed tapered periodogram by a moderate amount.* For short samples, $N \simeq 300$, the smoothed four taper analysis reduces the relative RMSE by 14 % in comparison with the adaptive multitaper and by 21 % in comparison with the smoothed tapered periodogram. Figure 13 plots

the normalized root mean square error, $RMSE(f) = |\widehat{Var}(f) + \hat{B}^2(f)|^{1/2}/S_{Con}(f)$. Figure 13 shows that the smoothed multitaper dominates the other estimators over the entire frequency range. Figure 14 plots the ratios of the RMSEs: $\frac{RMSE(MT)}{RMSE(SMT)}$ and $\frac{RMSE(SP)}{RMSE(SMT)}$ as a function of frequency. As N increases, the advantage of smoothed multitaper decreases, but is still apparent. For $N = 1000$, the smoothed five taper analysis reduces the relative RMSE by 7–8% in comparison with the adaptive multitaper and smoothed tapered periodogram.

We are uncertain as to exactly why the smoothed multitaper performs better. One explanation is that without smoothing, the multitaper kernel, $\sum_k |V_k(f)|^2$, has oscillatory sidelobes which becomes small at certain frequencies. Thus the unsmoothed taper is not using these frequencies effectively in the spectral estimate. By smoothing the multitaper estimate, we are averaging the multitaper kernel and thereby using the degrees of freedom in the frequencies where the unsmoothed sidelobes are very small.

For $N = 1000$, the sequential deselection estimate has an average relative error of 24 %, which is effectively the same as the RMSE for the smoothed periodogram with the Tukey taper. Thus the advantage of multitaper over the smoothed tapered periodogram is decreasing with N . Multitaper analysis has more efficiency, because each of the taper estimates $\hat{S}^{(k)}(f)$ is centered about the frequency of interest while the smoothed periodogram is essentially shifted spread an additional half Rayleigh frequency, $\frac{1}{N\Delta t}$ on each side. Thus the advantage of the multitaper will decrease with $\frac{1}{WN\Delta t}$, which measures the number of Rayleigh frequencies in the bandwidth.

VII. Summary and Recommendations

We have compared nonparametric estimators of the spectral density as measured by the RMSE error, normalized to the converged spectral estimate, and integrated over frequencies away from the spectral peaks at 1 MHz and 2 MHz. The smoothed four taper estimate outperforms the “pure” multitaper and the “pure” smoothed single taper periodogram. For $N = 300$, the adaptive multitaper has a 16 % larger RMSE, and the smoothed single taper periodogram has a 23 % larger RMSE. For $N = 1000$ and $N = 3000$, the smoothed multitaper estimate maintains an advantage, but the difference is decreasing.

Although we have only performed a detailed comparison on this particular dataset, we believe the relative ordering of the various methods is typical of data with smooth spectral densities which are at least partially resolved ($\frac{1}{N\Delta t} \ll$ characteristic frequency scalelength for spectral variation). The performance ratios of the methods depends critically on the amount of oversampling and on the spectral range. *We therefore recommend that a smoothed multitaper estimate with four to five different tapers be used in combination with the sequential deselection adaptive weighting. When possible, the kernel smoother should be data adaptive such that the kernel halfwidth decreases when the spectrum varies rapidly.*

Multitaper analysis uses all of the possible degrees of freedom in the bandwidth, $[f - W, f + W]$, while the smoothed tapered periodogram has its effective kernel support broadened by at least $\frac{1}{2N\Delta t}$ due to the spectral window support. As a result, multitaper analysis has a smaller bias than the smoothed tapered periodogram for a given variance. Since this additional broadening scales with the Rayleigh resolution, the advantage of multitaper decreases as N increases.

Another popular technique for spectral estimation, Welch’s method²⁹, divides the original time series into K separate pieces, and treats each segment as an independent realization. *When the segments are not overlapped, Welch’s method is an inefficient special case of multiple taper estimation.* By artificially separating adjacent subsegments, information is destroyed. Welch’s method is inefficient because the first K Slepian tapers are more strongly localized in frequency than the K tapered subsegments.

All of the spectral estimation methods reduce the variance of the estimate by effectively averaging over neighboring frequencies. Hence each method has an optimal bandwidth which minimizes the variance versus bias tradeoff. In our comparisons, the frequency bandwidths were chosen to minimize the integrated relative RMSE between the spectral estimate and the converged estimate using the 45,000 data point segment.

Another advantage of multitaper and smoothed multitaper analysis is that the

variance is estimated nonparametrically using jackknife resampling. Since the TFTR microwave fluctuations may be non-Gaussian in character, the only reliable estimate of the error bars is given by resampling. Similarly, the sequential deselection adaptive weighting is a nonparametric test to determine if the bias is sufficiently large to delete the last taper. In our comparison, sequential deselection outperformed the older adaptive weighting of Ref. 3 by up to 34 %.

Acknowledgements

We thank N. Bretz and R. Nazikian for many interesting discussions which stimulated this work and for detailed explanations of the physics of the TFTR microwave scattering experiment. KSR thanks C. Hurvich for extensive discussions and advice on time series analysis, and Alan Chave for providing his multitaper time series code. KSR & AS thank W. Sadowski and H. Weitzner for their support. We thank the TFTR group for collecting and allowing us to analyze the microwave scattering data. The referee's comments are gratefully acknowledged. The work of KSR and AS was funded by the U.S. Department of Energy Grant No. DE-FG02-86ER53223.

Appendix A: Maximally Frequency Localized Tapers

To minimize the bias error, associated with spectral leakage, we seek basis functions/tapers which are concentrated about the particular frequency of interest. Given a bandwidth W , the Slepian functions²¹, $V_k(f; N, W)$, are defined as the family of orthonormal solutions of the extremal problem: Maximize

$$\frac{\int_{-W}^W |V_k(f)|^2 df}{\int_{-1/2}^{1/2} |V_k(f)|^2 df} , \quad (A1)$$

subject to

$$V_k(f) = \sum_{n=-[\frac{N}{2}]}^{[\frac{N}{2}]} \nu_n^{(k)} e^{-2\pi i n f}. \quad (A2)$$

Equation A1 is most easily imposed by substituting Eq. (A2) directly into Eq. (A1), and solving the variational problem in the time domain. The first variation of Eq. (A1) yields the linear eigenvalue problem:

$$\sum_{n=-[\frac{N}{2}]}^{[\frac{N}{2}]} A_{mn}(N, W) \nu_n^{(k)} = \lambda_k \nu_m^{(k)} , \quad m = -[\frac{N}{2}], \dots, [\frac{N}{2}] , \quad (A3)$$

where the spectral concentration matrix, $\mathbf{A}(N, W)$, satisfies

$$A_{mn}(N, W) \equiv \int_{-W}^W e^{2\pi i(m-n)f} df = \frac{\sin 2\pi W(n-m)}{\pi(n-m)}. \quad (A4)$$

$\mathbf{A}(N, W)$ is a real symmetric matrix, and therefore, has a complete set of N orthonormal eigenvectors. In the Fourier domain, Eq. (A3) corresponds to

$$\int_{-W}^W D_N(f-f') V_k(f') df' = \int_{-W}^W \frac{\sin N\pi(f-f')}{\sin \pi(f-f')} V_k(f') = \lambda_k V_k(f). \quad (A5)$$

The eigenvalue, λ_k , is the ratio of the integral of $|V_k(f)|^2$ in $[-W, W]$ to $[-\frac{1}{2}, \frac{1}{2}]$, and thus is always positive and bounded by one. The Slepian functions are known as prolate spheroidal wavefunctions. The discrete prolate spheroidal sequences and the corresponding prolate spheroidal wavefunctions have a number of special properties:

a) The Slepian functions are orthonormal on the interval, $[-1/2, 1/2]$, and orthogonal on the interval, $[-W, W]$:

$$\int_{-1/2}^{1/2} V_k(f) V_{k'}(f) df = \delta_{k,k'}, \quad \int_{-W}^W V_k(f) V_{k'}(f) df = \lambda_k \delta_{k,k'}. \quad (A6)$$

b) The k th Slepian function has k zeros in the interval $(-W, W)$. Figure 15 displays the first four Slepian functions, $V_k(f; N, W)$, for $N = 100$.

c) $2NW$ eigenvalues, λ_k , are near one and the rest of the eigenvalues are near zero. This corresponds to the $4NW$ degrees of freedom in a band-limited signal of length N when the center frequency is not located within $\frac{1}{N\Delta t}$ of zero. Table 3 displays the eigenvalues versus the index k for $N = 300$.

d) The sum of squares of the first $2NW$ Slepian functions, $\sum_{k=1}^{2NW} |V_k(f; N, W)|^2$, converges to the characteristic function of the interval $(-W, W)$ as N increases: $\sum_{k=1}^{2NW} |V_k(f; N, W)|^2 \rightarrow \chi_{(-W, W)}(f)$. Figure 16 displays $\sum_{k=1}^{2NW} |V_k(f; N, W)|^2$.

e) The matrix, \mathbf{A} , commutes with a tridiagonal matrix with well separated eigenvalues. Thus the eigentapers, $\{\nu^{(k)}\}$, may be determined numerically by solving the eigenvalue equation of the tridiagonal matrix (see Appendix A in Ref. 6). As N tends to infinity, direct determination of the tapers through Eq. (A3) is exponentially ill-conditioned. For large taper lengths, the only successful numerical method for determining the Slepian eigentapers is to compute the eigenvectors of the commuting tridiagonal matrix.

Appendix B: Adaptive Taper Weightings

In this appendix, we derive three adaptive weightings for the multiple taper estimate – sequential deselection, minimum expected error weighting, and Thomson’s Wiener filter weighting. Our analysis assumes that the spectrum varies slowly on the scale of the taper bandwidth W . Formally, we expand the properties of the multitaper estimates in powers of $\frac{S''(f)W^2}{S(f)}$. A generalization of Eq. (12) shows that the spectral estimates from two different orthogonal taper are uncorrelated to $O\left(\left|\frac{WS'(f)}{S(f)}\right|^2\right)$.

We decompose the bias of the k th spectral estimate into the narrow banded part from $|f' - f| < W$ and the broad-banded part. To second order in W , we have

$$\mathbf{E}[\hat{S}^{(k)}(f)] = S(f)\lambda_k + S''(f)D_k + \oint |V_k(f - f')|^2 S(f') df' , \quad (B1)$$

where $\oint \equiv \int_{-1/2}^{-W} + \int_W^{1/2}$ and $D_k = \int_{-W}^W f'^2 |V_k|^2(f') df'$. From the Cauchy inequality applied directly to Eq. (13), we have

$$\int df \oint |V_k(f - f')|^2 S(f') df' \leq \sigma^2(1 - \lambda_k) . \quad (B2)$$

Thus we approximate the broad-band bias by replacing the local value of the integral with its average value, which yields the approximation:

$$\mathbf{E}[\hat{S}^{(k)}(f)] \sim S(f)\lambda_k + S''(f)D_k + \sigma^2(1 - \lambda_k) . \quad (B3)$$

If $S''(f)$ is known or estimated, we can correct the k th spectral estimate: $\hat{S}_{new}^{(k)}(f) = \hat{S}_{old}^{(k)}(f) - S''(f)D_k$. This estimator is unbiased to $O(W^4)$, and therefore, corresponds to higher order kernel estimators. In the absence of knowledge about $S''(f)$, we will consider only the approximate bias given by $\sigma^2(1 - \lambda_k)$.

As Table 3 indicates, $1 - \lambda_k$ is usually very small except for the last several tapers with $k \sim 2NW$. Therefore, a likely failure mode for multitaper estimation is that the last couple of spectral estimates, $\hat{S}^{(k \sim 2NW)}$, are systematically larger than the other spectral estimates due to broad-banded bias. Our first adaptive weighting is called sequential deselection and is designed to suppress this failure mode.

In *sequential deselection*, we begin by computing the mean and standard deviation of the first $K - 1$ tapers. We then require the last spectral estimate to satisfy the one sided F-test: $S^{(K)}(f) \leq \bar{S}(f) + \alpha_K \hat{\sigma}(f)$. If the K th estimate fails the test, we delete it and repeat the test on the next to last estimate. (We recompute $\bar{S}(f)$ and $\hat{\sigma}(f)$ using only the first $K - 2$ tapers.) We modify this basic testing procedure in two ways. First, we require that no more than 20 % of the estimates are deleted. Second, we recognize that $S^{(K)}(f)$ may pass the test due to random chance and that the $K - 1$ estimate may be bad. Therefore, we automatically test the $K - 1$ estimate using the same

one-sided test even when $S^{(K)}(f)$ passes the test. We require that two consecutive spectral estimates pass the one-sided test before terminating the testing procedure. In practice, we find that only rarely are more than two estimates discarded. Near the spectral peaks, the adaptive estimates use all of the estimates.

The second and third adaptive weightings assume that the broad-banded bias is important and distributed evenly in the exterior domain. Thus these adaptive weightings use the bias model: $E[\hat{S}^{(k)}(f)] \sim S(f)\lambda_k + \sigma^2(1 - \lambda_k)$. The expected square error of the adaptive weighting of Eq. (15) is

$$\left[\left(\sum_{k=0}^{K-1} c_k(f) (S(f)\lambda_k + \sigma^2(1 - \lambda_k)) - S(f) \right) \right]^2 + \sum_{k=0}^{K-1} c_k(f)^2 (S(f)\lambda_k + \sigma^2(1 - \lambda_k))^2, \quad (B4)$$

where the first term is the square bias and the second term is the Gaussian estimate of the variance. Minimizing Eq. (B4) with respect to c_k yields the *minimum expected error adaptive weighting*:

$$c_k(f) = \frac{1}{K+1} \left(\frac{1}{\lambda_k + \frac{\sigma^2}{S(f)}(1 - \lambda_k)} \right). \quad (B5)$$

Thus $c_k(f)$ downweights the last tapers, ($k = K, K-1$), when $\sigma^2(1 - \lambda_k) \gg S(f)$.

In Refs. 3 & 6, Thomson advocates a *Wiener filter weighting* for c_k :

$$g_k(f) = \frac{1}{K} \left(\frac{\lambda_k}{\left[\lambda_k + \frac{\sigma^2}{S(f)}(1 - \lambda_k) \right]^2} \right), \quad c_k(f) \equiv \frac{K g_k(f)}{\sum_{k=0}^{K-1} g_k(f)}. \quad (B6)$$

Thomson's $g_k(f)$ minimizes the expected error in estimating $dZ(f)$ instead of $S(f)$. The normalizing factor, $K / \sum_{k=0}^{K-1} g_k(f)$, forces the adaptive weighting to be unbiased when $S(f) \equiv \sigma^2$ at the cost of having a larger expected error. Equation (B6) downweights the last tapers more than the optimal weighting of Eq. (B5). Thus the weighting of Eq. (B6) is more conservative since it more strongly downweights the more questionable $S^{(k)}$ and this gives it more robustness.

The second and third adaptive weightings essentially assume that the spectrum is equal to $S(f)$ for $|f' - f| \leq W$ and $S(f') = \frac{\sigma^2 - 2wS(f)}{1 - 2W}$ for $|f' - f| > W$. This is a good assumption when the spectrum is roughly constant over most of the domain and has local regions of much smaller amplitude. Unfortunately, the more typical case is that the spectrum has local regions of much *larger* amplitude. In this case, the extent of the adaptive weighting should depend on the distance to the spectral peaks. For the TFTR data at large frequencies, $|f| > 1.7$ MHz, the broad-banded bias predominately comes from the remote spectral peak at 1 MHz. Thus the correction

to the denominator of Eq. (B5) should be $\frac{\sigma^2}{S(f)}|V_k(f - 1MHz)|^2$ instead of $\frac{\sigma^2}{S(f)}(1 - \lambda_k)$. By using $(1 - \lambda_k)$ instead of $|V_k(f - 1MHz)|^2$, we overcorrect for the broad-banded bias. The same overcorrection is present in Thomson's (B6) weighting; however, the normalizing factor reduces the bias at the cost of increasing the variance by not downweighting the last tapers too much.

The minimum expected error adaptive weighting is optimal only for the assumed spectrum. The weak point of our analysis is that we treat $S(f)$ as given and not estimated. *In practice, the weights, $c_k(f)$, are computed iteratively using the previous estimate of $S(f)$. Thus the total spectral estimate is nonlinear in $|y(f)|^2$.*

Appendix C: Jackknife Estimates

The jackknife is a statistical “resampling” technique^{18–20} to estimate the bias and variance of complicated estimators, $\hat{\theta} = T_K(y_1, \dots, y_K)$. For simplicity, we assume the y_ℓ are independent and identically distributed, and that the estimator $\hat{\theta}_K$ is a symmetric function in its K arguments. The jackknife begins by estimating θ from the K different delete-one samples:

$$\hat{\theta}_{(\bar{\ell})} \equiv T_{K-1}(y_1, \dots, y_{\ell-1}, y_{\ell+1}, \dots, y_K) \quad . \quad (C1)$$

The jackknife reduces the bias by Aitken extrapolation. We assume that $\hat{\theta}$ has a bias proportional to $\frac{1}{K}$ and $\hat{\theta}_{(\bar{\ell})}$ has a bias proportional to $\frac{1}{K-1}$. We define the ℓ -th pseudo-value:

$$p_\ell = K\hat{\theta} - (K-1)\hat{\theta}_{(\bar{\ell})} \quad . \quad (C2)$$

The bias proportional to $\frac{1}{K}$ has been eliminated from the pseudo-value. When the bias has a Taylor series expansion in $\frac{1}{K}$, the pseudo-values have biases proportional to $\frac{1}{K^2}$. The jackknife estimate of θ is the average of the K pseudo-values

$$\tilde{\theta} = \frac{1}{K} \sum_{i=1}^K p_i = K\hat{\theta} - \frac{K-1}{K} \sum_{\ell=1}^K \hat{\theta}_{(\bar{\ell})} \quad . \quad (C3)$$

The jackknife reduces the bias of the estimate, but in general raises the variance of the estimate. The jackknife estimates the variance of $\tilde{\theta}$ by assuming the pseudo-values, p_ℓ , are independent estimates of θ :

$$\hat{\sigma}_{jack}^2 = \mathbf{Var} [\tilde{\theta}] = \frac{1}{K(K-1)} \sum_{\ell=1}^K (p_\ell - \tilde{\theta})^2 = \frac{K-1}{K} \sum_{\ell=1}^K (\hat{\theta}_{(\bar{\ell})} - \hat{\theta}_{(\cdot)})^2 \quad , \quad (C4)$$

where

$$\hat{\theta}_{(\cdot)} \equiv \frac{1}{K} \sum_{\ell=1}^K \hat{\theta}_{(\bar{\ell})}$$

is the arithmetic mean.

As K increases, $\frac{\tilde{\theta} - \theta}{\hat{\sigma}_{jack}}$ tends asymptotically to a T distribution. The convergence is often slow, and therefore “variance stabilizing” transformations^{20,30}, such as the logarithmic transformation for spectral estimation, are applied to the delete-one estimates $\hat{\theta}_{(\bar{\ell})} \rightarrow g(\hat{\theta}_{(\bar{\ell})})$ before jackknifing.

In particular, we wish to estimate $\ln(S(f))$ and the *variance* of the estimate, given K multitaper estimates. $\ln[\hat{S}^{(k)}(f)]$ has two sources of bias error. First, there is bias because $E[\hat{S}^{(k)}(f)]$, as given by Eq. (6), is not equal to $S(f)$. For fixed k , this bias

goes to zero as $N \rightarrow \infty$. Neglecting this effect, $\hat{S}^{(k)}(f)$ has a χ_2^2 (or exponential) distribution, and so has its most probable value at zero. As a result, the distribution of its logarithm has a very long lower tail. This lower tail causes a second, more serious type of bias in the estimate of $\ln[\hat{S}^{(k)}(f)]$: $\mathbf{E}[\ln(\hat{S}^{(k)})] = \ln(S) - 0.577$. To reduce this bias, we average the K estimates prior to taking the logarithm: $\bar{\hat{S}} \equiv \frac{1}{K} \sum_{k=0}^{K-1} \hat{S}^{(k)}(f)$. $\bar{\hat{S}}$ has a χ_{2K}^2 distribution and the expectation of its logarithm is given by

$$\mathbf{E}[\ln(\bar{\hat{S}})] = \ln(S) + B_\chi(K) , \quad (C5)$$

where the bias, $B_\chi(K)$, is given by

$$B_\chi(K) = \psi(K) - \ln(K) , \quad (C6)$$

with ψ being the digamma function. Thus the bias goes to zero as $\frac{1}{K}$. Similarly, the variance of $\ln(\bar{\hat{S}})$ is

$$\mathbf{Var}[\ln(\bar{\hat{S}})] = \psi'(K) , \quad (C7)$$

where ψ' is the trigamma function. Equation (18) computes the mean of the $\ln[\hat{S}^{(k)}(f)]$ rather than the logarithm of the mean. Its variance is

$$\mathbf{Var}[\overline{\ln(\hat{S})}] = \frac{1}{K} \psi'(1) = \frac{\pi^2}{6K} . \quad (C8)$$

Table 4 shows that the variance of $\ln[\bar{\hat{S}}]$ is lower than that of $\overline{\ln(\hat{S})}$. In Table 4, both quantities are given in column 3 and 6 respectively. Column 2 gives the bias of $\ln[\bar{\hat{S}}]$, which compares favorably with $\frac{.577}{K}$, the bias of $\ln(\hat{S})$.

Equations (C5)-(C8) are all based on the assumption that the stochastic process is Gaussian. When the Gaussian assumption is questionable, the variance needs to be estimated empirically. To minimize the effects of the long tail of $\ln(\hat{S}^{(k)})$, we use the jackknife estimate. For the log-spectral estimate, Eq. (C1) becomes

$$\hat{\theta}_{(\bar{\ell})} = \ln[\hat{S}_{(\bar{\ell})}(f)] = \ln \left[\frac{1}{K-1} \sum_{k=0, k \neq \ell}^{K-1} \hat{S}^{(k)}(f) \right] . \quad (C9)$$

The jackknife variance become

$$\hat{\sigma}_J^2 = \frac{K-1}{K} \sum_{\ell=0}^{K-1} \left[\ln[\hat{S}_{(\bar{\ell})}(f)] - \ln[\hat{S}_{(\gamma)}(f)] \right]^2 , \quad (C10)$$

where

$$\ln(\hat{S}_{(\gamma)}) = \frac{1}{K} \sum_{\ell=0}^{K-1} \ln[\hat{S}_{(\bar{\ell})}(f)] . \quad (C11)$$

When the process is Gaussian, the expectation of jackknife variance estimate is

$$\mathbf{E}[\hat{\sigma}_J^2] = \frac{(K-1)^2}{K} \left[\frac{2}{(K-2)^2} + \frac{1}{2} \left[\psi'(\frac{K-1}{2}) - \psi'(\frac{K-2}{2}) \right] \right] . \quad (C12)$$

The derivation of Eq. (C12) is complicated and will be presented elsewhere. Asymptotically, Eq. (C12) reduces to

$$\mathbf{E}[\hat{\sigma}_J^2] \sim \frac{(K-1)^2(K-3)}{K(K-2)^3} . \quad (C13)$$

In Table 4, Column 4 gives the expectation of the jackknife variance estimate, σ_J^2 , and column 5 gives its asymptotic form for large K . Thus, the jackknife variance estimate slightly overestimates the actual variance, $\psi'(K)$. Column 7 gives the ratio of column 6 to column 4 and shows the superiority of the jackknife estimate.

Appendix D: Empirical estimation of the expected error

The average square error consists of two pieces, the variance and the square bias. The true spectrum is unknown, and therefore, we estimate it using the entire 45,000 point segment with a bandwidth of 14 kHz, corresponding to 500 degrees of freedom. Figure 5 illustrates that the multitaper estimate and the smoothed periodogram are nearly identical. We will treat the adaptive multitaper estimate using sequential deselection as the converged value of the true spectrum, $S_{Con}(f)$. To quantify the difference, we compute the difference of the two estimates in Fig. 5 divided by the multitaper estimate, $\frac{S_{SP}(f)}{S_{MT}(f)} - 1$, where the subscripts, MT and SP , stand for multitaper and smoothed Tukey tapered periodogram respectively. We find that on average the two estimates seldom differ by less than 1.1 percent.

We estimate the bias of the various methods by

$$\hat{B}(f) = \frac{1}{N_s} \sum_{i=1}^{N_s} \hat{S}_i(f) - S_{Con}(f) . \quad (D1)$$

Our estimate of the bias neglects the error in $S_{Con}(f)$ and assumes that the spectrum is stationary. We expect that the square bias is proportional to W^4 and that the variance is inversely proportional to the number of degrees of freedom. Thus the error in the 300 point estimates is much larger than that of the 45,000 point estimate. The assumption of stationarity is less valid. Figure 17 plots the multitaper estimates with $W = 20$ kHz for the first third, the second third and the final third of the data segment. Differences are visible only at the secondary maximum at $550 \text{ kHz} \pm 100 \text{ kHz}$. Physically, this is interesting because this secondary maximum represents the dominant drift wave frequencies. Thus the electron drift wave fluctuation level is growing on the ten millisecond time scale. In Ref. 11, we explore nonstationary plasma fluctuations. For the purpose of this article, the examination of stationary spectra, our empirical convergence study may not be relevant in the 400–600 kHz frequency range.

To reduce the influence of nonstationarity on our estimate of the variance, we compare $\hat{S}_i(f)$ with the average of $\hat{S}_{i-1}(f)$ and $\hat{S}_{i+1}(f)$:

$$\widehat{Var}(f) = \frac{2}{3(N_s - 2)} \sum_{i=2}^{N_s-1} \left(\hat{S}_i(f) - \frac{\hat{S}_{i-1}(f) + \hat{S}_{i+1}(f)}{2} \right)^2 , \quad (D2)$$

where we use nonoverlapping subsegments to compute the variance.

Bibliography

1. A.J. Wooten, B.A. Carreras, H. Matsumoto, K. McGuire, W.A. Peebles, Ch.P. Ritz, P.W. Terry, S.J. Zweben, Phys. Fluids B, **2**, 2879 (1990).
2. P. Liewer, Nucl. Fusion **25**, 543 (1985).
3. D.J. Thomson, Spectrum estimation and harmonic analysis. Proc. I.E.E.E., **70**, 1055 (1982).
4. D.J. Thomson and A.D. Chave, in *Advances in spectrum analysis*, edited by S. Haykin, (Prentice-Hall, New York 1990) Ch. 2, pg. 58-113.
5. C.T. Mullis and L.L. Scharf, in *Advances in spectrum analysis*, edited by S. Haykin, (Prentice-Hall, New York 1990) Ch. 1, pg. 1-57.
6. D.J. Thomson, Phil. Trans. R. Soc. Lond. A, **332**, 539 (1990).
7. J. Park, C.R. Lindberg, and F.L. Vernon, J. Geophys. Res., **92B**, 12,675 (1987).
8. M.B. Priestley, *Spectral analysis and time series*. (Academic Press, New York 1981).
9. L.H. Koopmans, *The spectral analysis of time series*. Ch. 8, (Academic Press, New York 1974).
10. U. Grenander and M. Rosenblatt, *Statistical analysis of stationary time series*. (Wiley, New York 1957).
11. K.S. Riedel, A. Sidorenko, N. Bretz, D.J. Thomson, Spectral density estimation of plasma fluctuations II: Nonstationary analysis of ELM spectra. Published in this issue, Physics of Plasmas **1** page ? (1994).
12. C.P. Ritz, E.J. Powers and R.D. Bengtson, Phys. Fluids B **1**, 153 (1989).
13. D.J. Grove and D.M. Meade, Nuclear Fusion **25**, 1167 (1985).
14. N. Bretz, P. Efthimion, J. Doane, and A. Kritiz, Rev. Sci. Instr. **59**, 1538 (1988).
15. N. Bretz, R. Nazikian, W. Bergin, M. Diesso, J. Felt, M. McCarthy, Rev. Sci. Instr. **61**, 3031 (1990).

16. N. Bretz, R. Nazikian, and K. Wong, *Proceedings of the 17th European Phys. Soc. Conf.*, (European Phys. Soc., Amsterdam, 1990) p. 1544.
17. R. Nazikian, N. Bretz, E. Fredrickson, Y. Nagayama, E. Mazzucato, K. McGuire, H.K. Park, G. Taylor, A. Cavallo, M. Diesso, J. Felt, *Proceedings of the 18th European Phys. Soc. Conf.*, (European Phys. Soc., Berlin 1991) Vol. I p. 265.
18. R. Miller, *Biometrika*, **61**, 1 (1974).
19. C.F.J. Wu, *Ann. Stat.*, **14**, 1261 (1986).
20. N. Cressie, *J. Roy. Stat. Soc. B*, **43**, 177 (1981).
21. D. Slepian, *Bell Syst. Tech. J.*, **57**, 1371 (1978).
22. J. Sheffield, *Plasma Scattering of Electromagnetic Radiations*. (Academic Press, New York, 1975).
23. N. Bretz, *Plasma Phys.* **38**, 279 (1987).
24. T.P. Hughes and S.R.P. Smith, *Plasma Phys.* **42**, 215 (1989).
25. Y.J. Kim, K.W. Gentle, Ch. P.Ritz, T.L. Rhodes, R.D. Bengston, *Phys. Fluids B* **3** 674 (1991).
26. C. Hurvich, *Biometrika*, **75**, 485 (1988).
27. W. Haerdle, *Applied nonparametric regression*. (Cambridge University Press, Cambridge, New York, 1990).
28. H.G. Mueller, and U. Stadtmueller, *Annals of Statistics*, **15**, 182(1987).
29. P.D. Welch, *I.B.M J. Research Devel.* **5**, 141 (1961).
30. R.G.Miller, *Ann. Math. Statist.*, **61**, 567 (1968).

k	λ_k	$1 - \lambda_k$
0	0.999999999999996	$3.62 \cdot 10^{-14}$
1	0.9999999999995	$4.65 \cdot 10^{-12}$
2	0.9999999997	$2.90 \cdot 10^{-10}$
3	0.9999999989	$1.14 \cdot 10^{-8}$
4	0.9999997	$3.18 \cdot 10^{-7}$
5	0.999993	$6.60 \cdot 10^{-6}$
6	0.99989	$1.05 \cdot 10^{-4}$
7	0.9987	$1.31 \cdot 10^{-3}$
8	0.9875	$1.25 \cdot 10^{-2}$
9	0.9157	$8.43 \cdot 10^{-2}$

Table 3: Eigenvalues for $N = 300, W = 91$ kHz

K	$\text{Bias}_\chi(K)$	$\psi'(K)$	Eq. (C12)	Eq.(C13)	Eq. (C8)	$\frac{\text{Eq. C8}}{\text{Eq. C12}}$
3	0.17582	0.39493	0.47342	0.00000	0.54831	1.15818
4	0.13017	0.28382	0.32610	0.28125	0.41123	1.26105
5	0.10332	0.22132	0.24732	0.23703	0.32898	1.33019
6	0.08564	0.18132	0.19879	0.19531	0.27415	1.37905
7	0.07312	0.15354	0.16605	0.16457	0.23499	1.41515
8	0.06380	0.13313	0.14251	0.14178	0.20561	1.44279
9	0.05658	0.11751	0.12479	0.12439	0.18277	1.46459
10	0.05083	0.10516	0.11097	0.11074	0.16449	1.48220
11	0.04614	0.09516	0.09991	0.09976	0.14953	1.49671
12	0.04224	0.08690	0.09084	0.09075	0.13707	1.50887
13	0.03895	0.07995	0.08329	0.08322	0.12653	1.51919
14	0.03613	0.07404	0.07689	0.07684	0.11749	1.52807
15	0.03370	0.06893	0.07140	0.07137	0.10966	1.53578
16	0.03157	0.06449	0.06664	0.06662	0.10280	1.54254
17	0.02970	0.06058	0.06248	0.06246	0.09676	1.54852
18	0.02803	0.05712	0.05881	0.05879	0.09138	1.55384
19	0.02654	0.05404	0.05554	0.05553	0.08657	1.55860
20	0.02520	0.05127	0.05262	0.05261	0.08224	1.56290

Table 4: Jackknife Log-spectral Estimates

Column 1 gives K , the number of tapers in the spectral estimate. Column 2 gives the bias of $\ln(\hat{S})$ for K tapers and column 3 gives its variance. Column 4 gives the expectation of the jackknife variance estimate, σ_J^2 , and column 5 gives its asymptotic form for large K . Column 6 gives the variance of the estimate of Eq. (18). Column 7 gives the ratio of column 6 to column 4 and shows the superiority of the jackknife estimate.

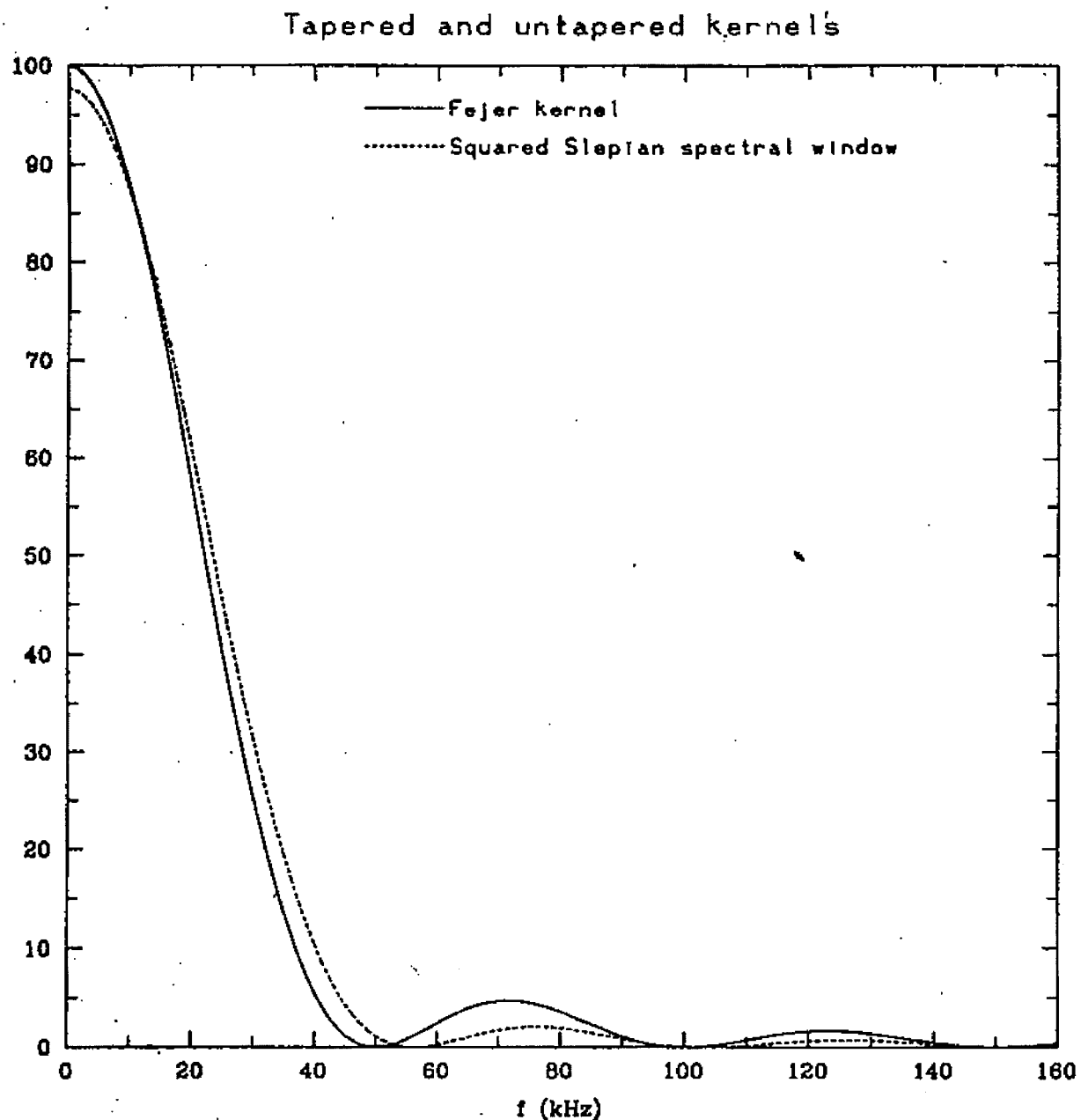


FIG. 1. Comparison of tapered and untapered kernels for $N=100$: The central lobe of the tapered kernel is broader than the Fejér kernel while the sidelobes are reduced. Solid line: Fejér kernel, $[\sin(N\pi f)/\sin(\pi f)]^2/N$, vs f . Dashed line: Squared amplitude of Slepian spectral window, $|V(f)|^2$, versus f for $\bar{W}=0.6$ ($W=30$ kHz).

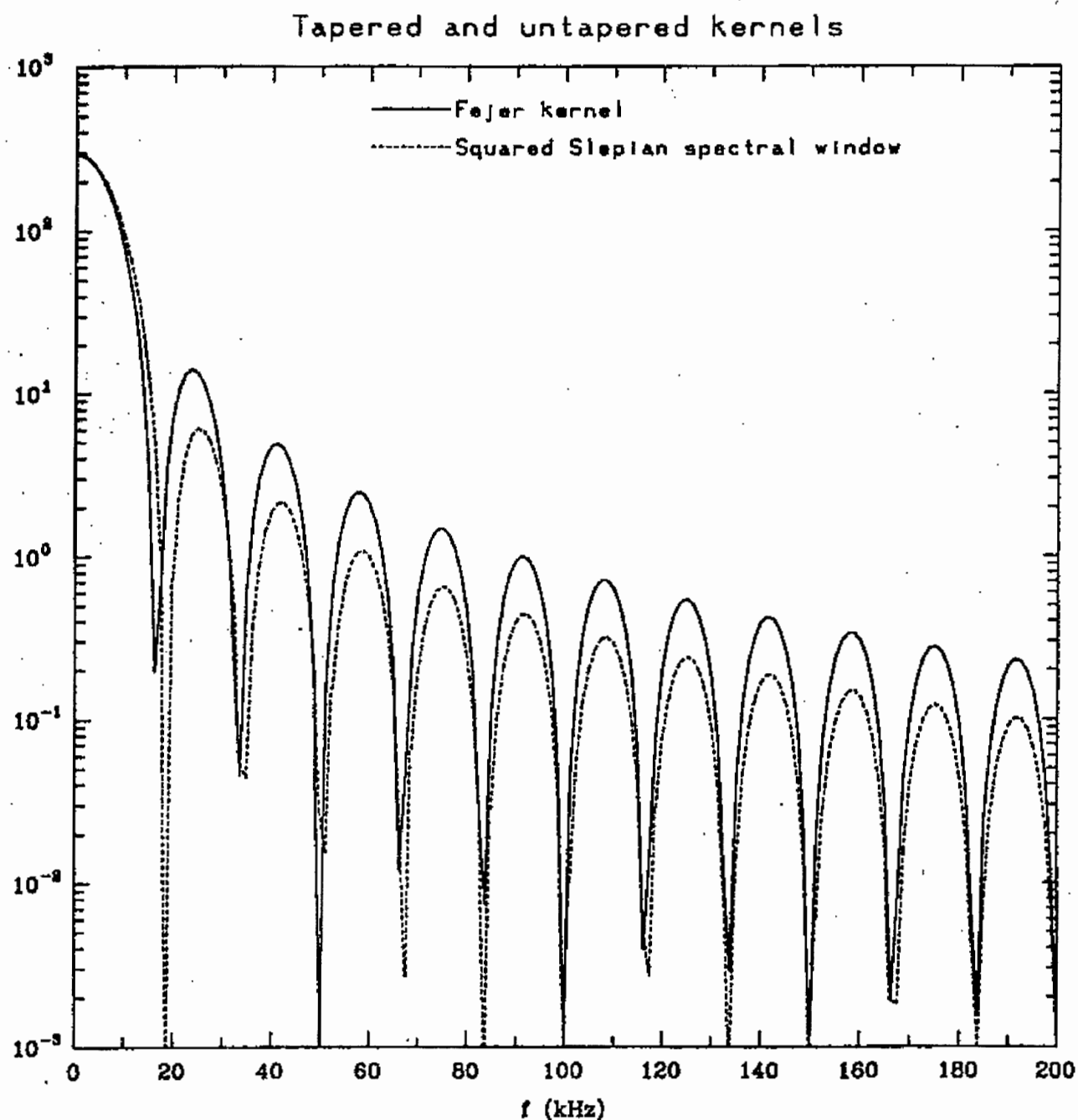


FIG. 2. Fejér kernel and squared Slepian spectral window $\bar{W}=0.6$ ($W = 10$ kHz), log scale for $N=300$. Both the tapered and untapered kernels decay as f^{-2} . The amplitude of the tapered sidelobes is reduced proportional to $\exp(-NW)$ relative to the Fejér kernel.

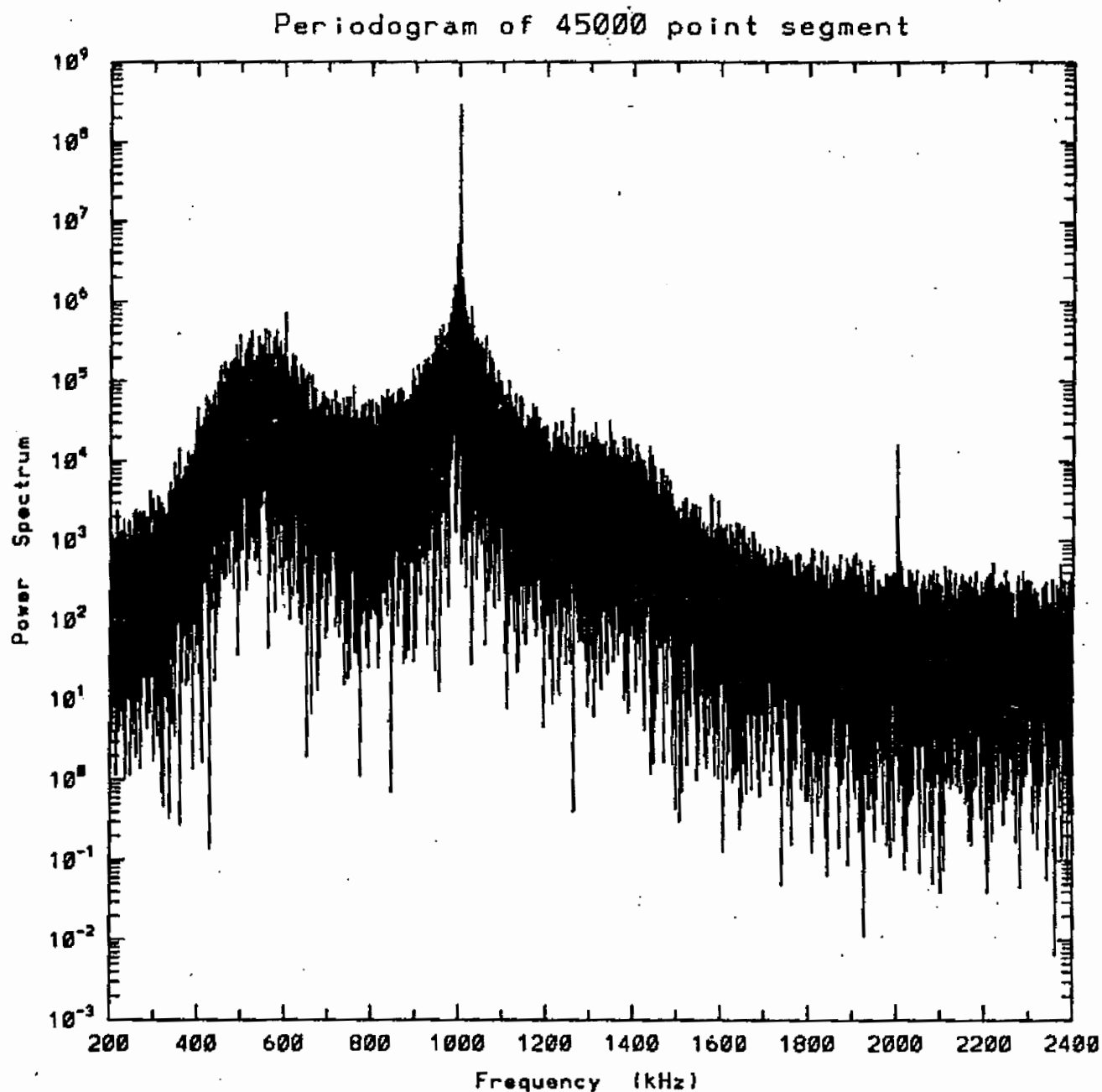


FIG. 3. Periodogram of entire 45 000 point segment, log scale. The rapid oscillations occur because the point estimates, $|y(f)|^2$, are nearly uncorrelated at frequencies of $1/(N\Delta t)$ apart. If the fluctuations were Gaussian and resolved in frequency, the periodogram would have a χ^2_2 distribution.

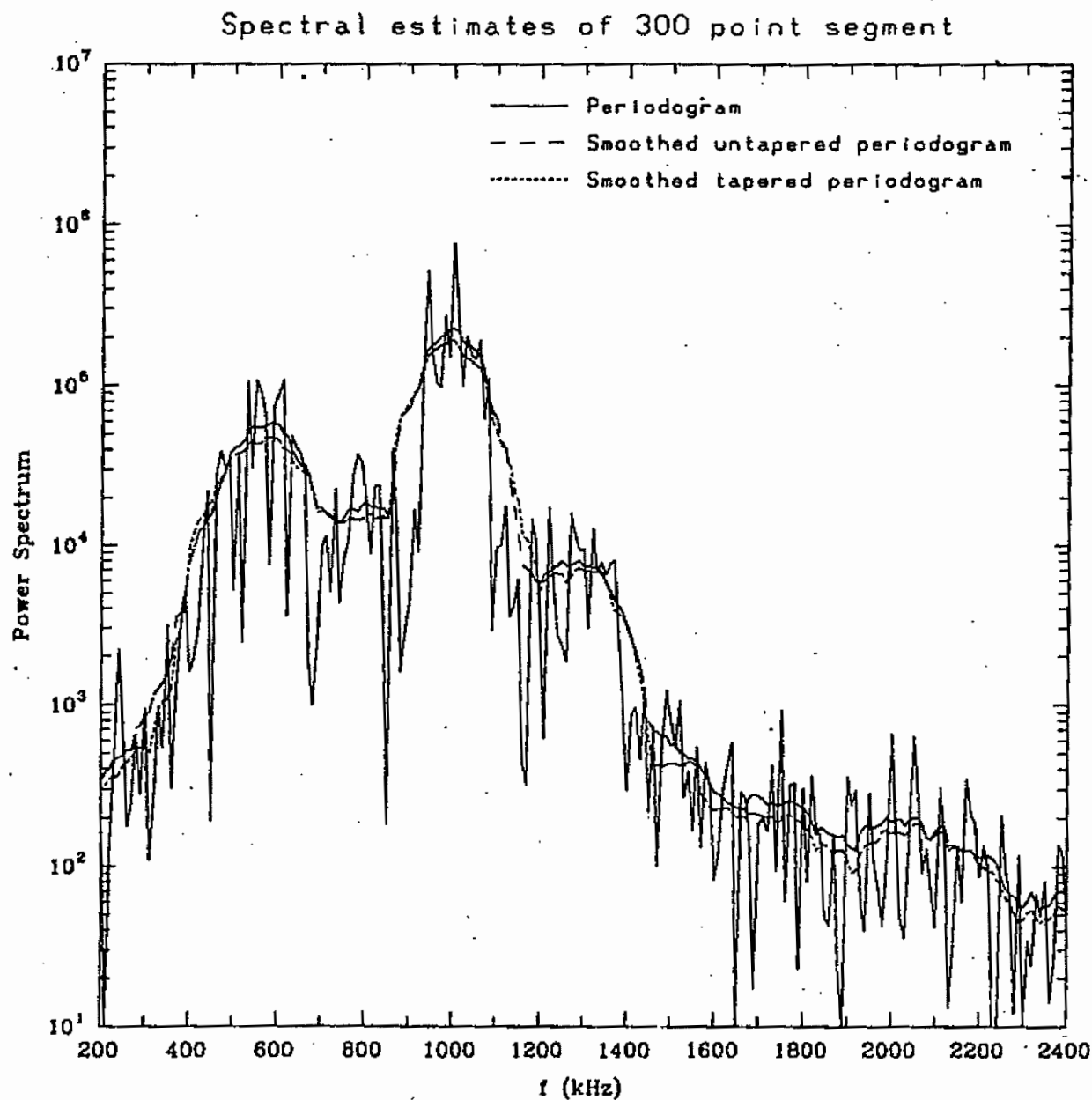


FIG. 4. Spectral estimates of 300 point segment beginning at $t=8.6$, log scale. The high variance of the unsmoothed periodogram obscures the systematic differences due to tapering. Solid line: Periodogram. Dashed line: Smoothed periodogram with $W=70$ kHz. Dotted line: Smoothed tapered periodogram with $W=70$ kHz using the Tukey split cosine taper with $\alpha N=33$.

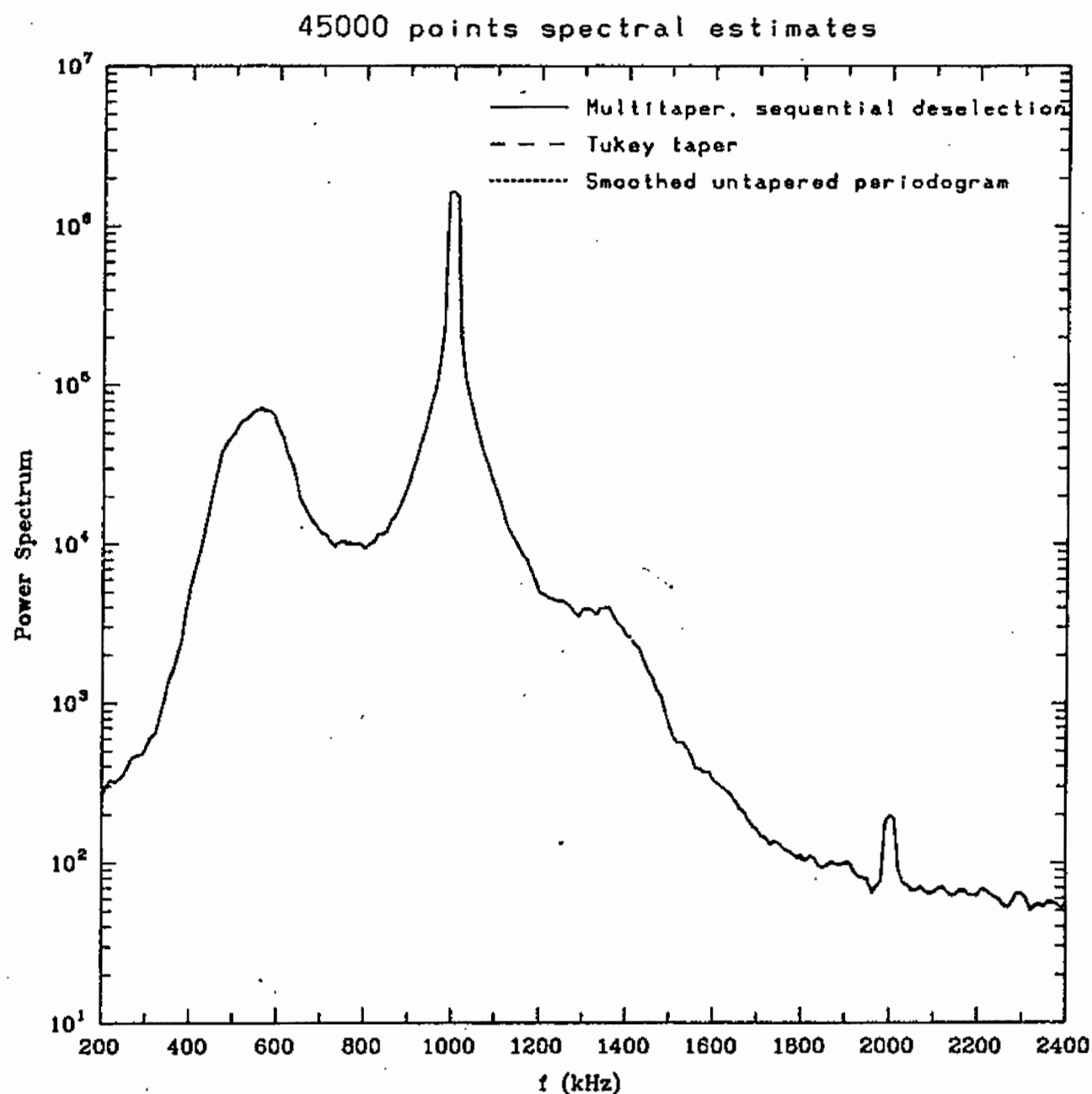


FIG. 5. Smoothed spectrum of entire 45 000 point segment, $W=14$ kHz. The central peak at 1 MHz is partially coherent and is believed to be due to fluctuations at the plasma edge. The secondary peak at 550 kHz is generated by fluctuations which are propagating in the electron drift direction. These fluctuations have a frequency spread of ± 100 kHz. Solid line: Multitaper estimate with sequential deselection. Dashed line: Tukey split cosine taper with $\alpha N = 100$. Dotted line: Periodogram.

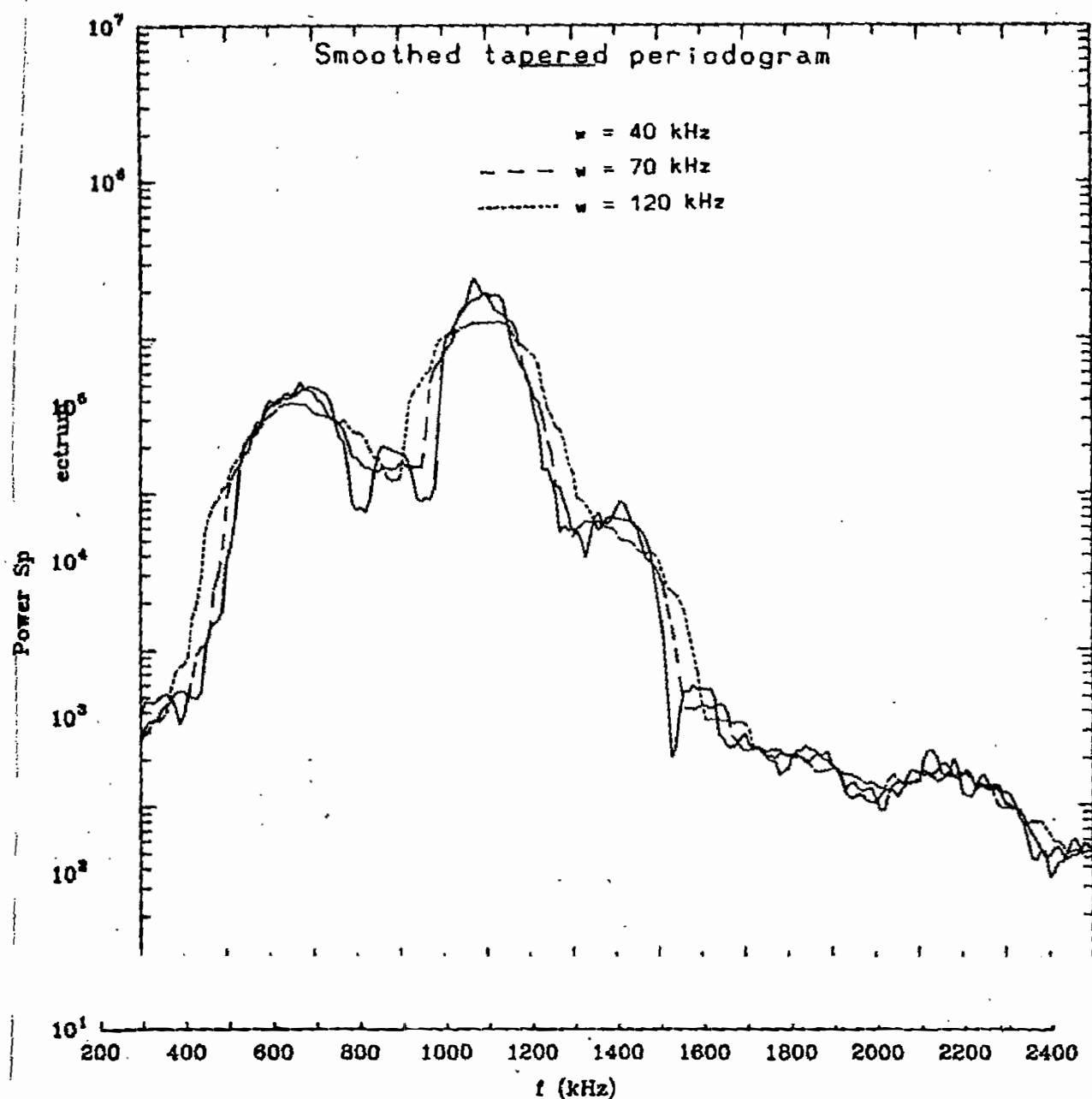


FIG. 6. Smoothed tapered periodogram for the 300 point subsegment of Fig. 4 for three different kernel half-widths, 40, 70, 120 kHz. As the kernel half-width increases, the spectrum is smoothed and artificially broadened. The area under the 1 MHz peak is approximately conserved. Solid line: $W=40$ kHz. Dashed line: $W=70$ kHz. Dotted line: $W=120$ kHz.

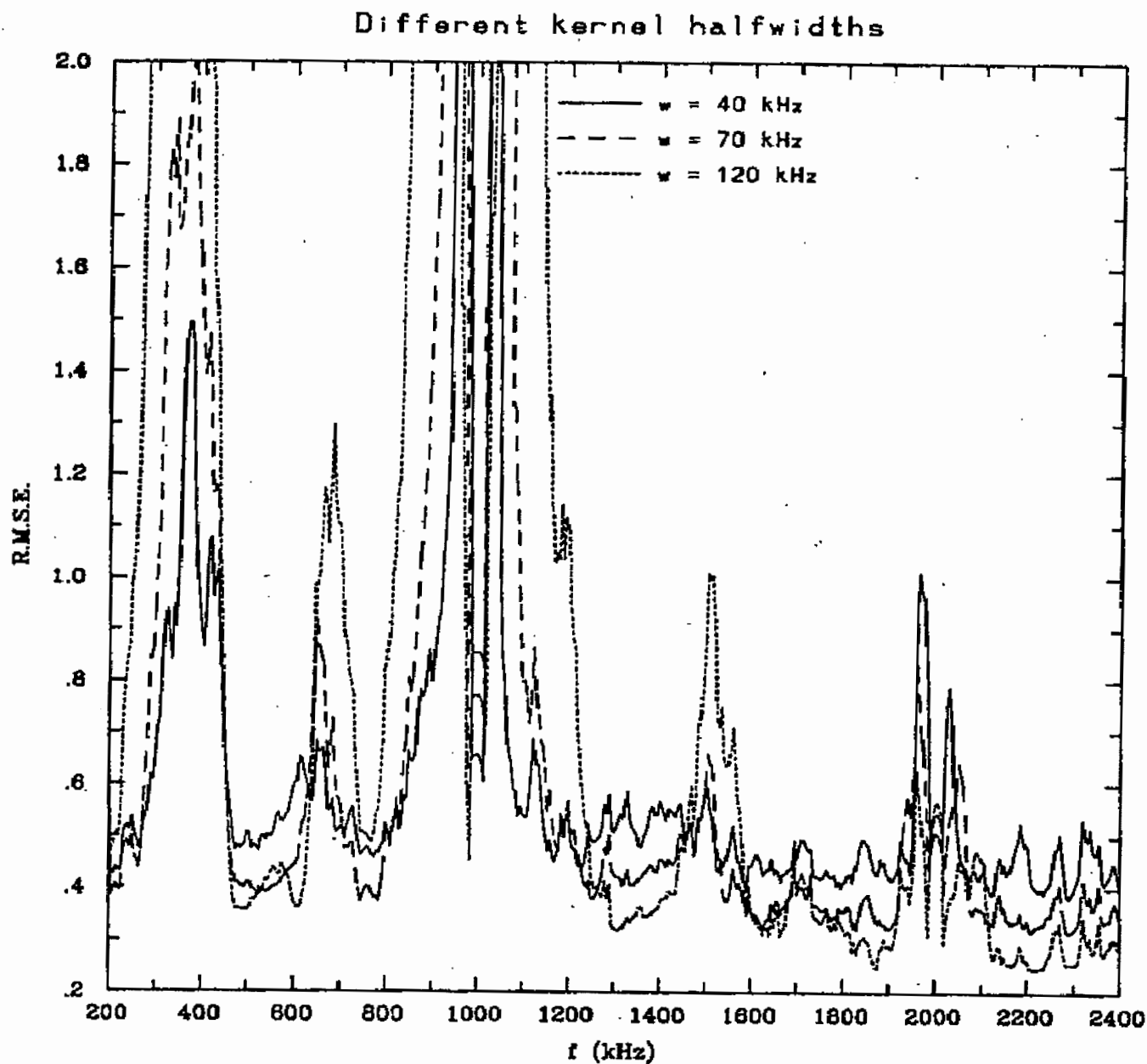


FIG. 7. Relative RMSE of the three different kernel halfwidths, averaged over 299 different subsegments. The calculation of the RMSE is described in the text. $w = 40$ kHz: deepest at the spectral peaks. $w = 120$ kHz: highest at the spectral peaks.

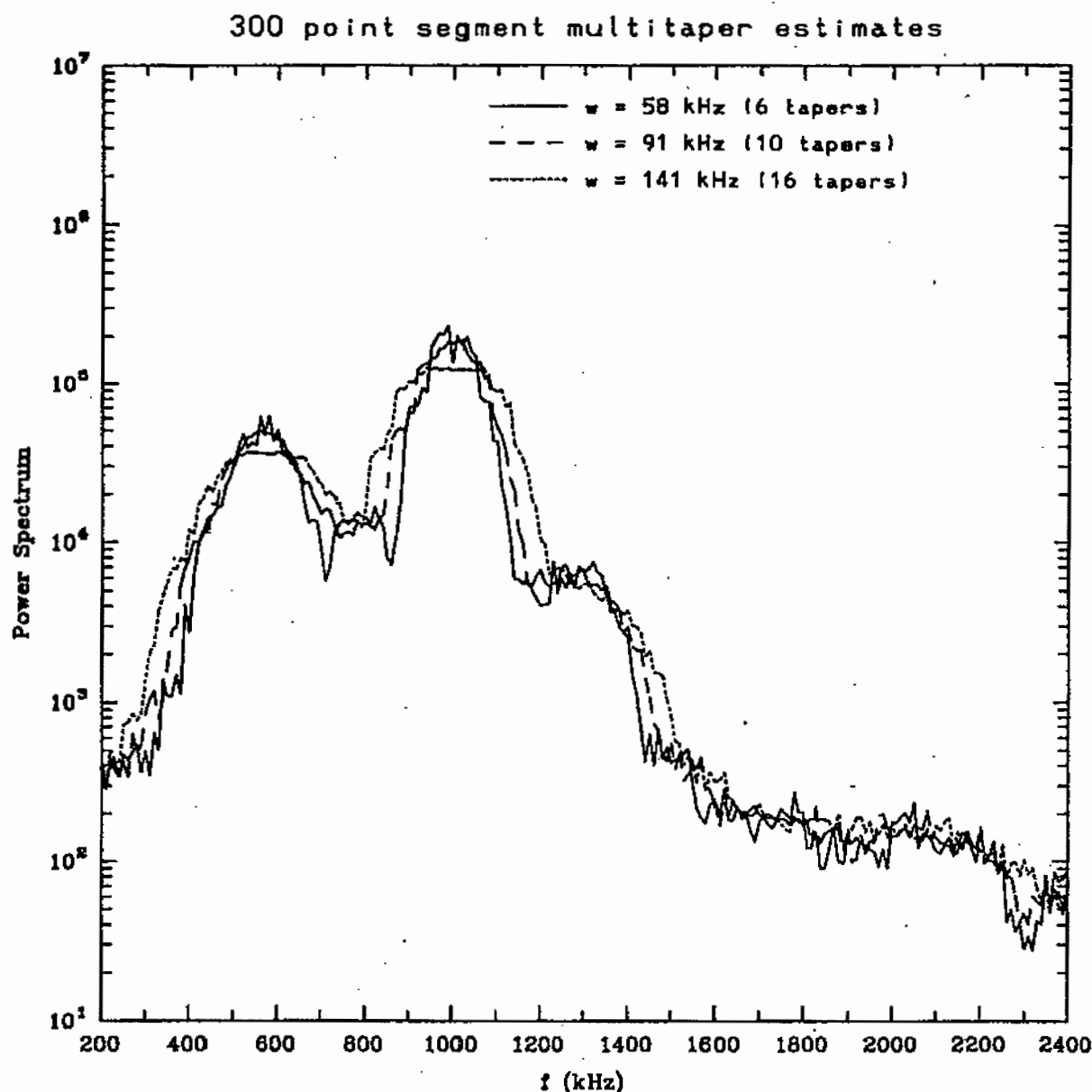


FIG. 8. Adaptive multiple taper spectral estimate of 300 point segment beginning at $t=8.6$. Figures 6 and 8 are similar, showing that choosing the correct bandwidth is the most important aspect of spectral estimation. For the same "official" bandwidth, the effective bandwidth of the smoothed tapered periodogram is larger than that of the multitaper estimate. This additional broadening is proportional to the Rayleigh resolution. For $N=300$, the Rayleigh resolution frequency, $1/(300\Delta t) \approx 17$ kHz, is a significant fraction of the spectral estimation half-width. Thus we use slightly larger bandwidths for the multitaper estimate. Solid line: $W = 58$ kHz. Dashed line: $W = 91$ kHz. Dotted line: $W = 141$ kHz.

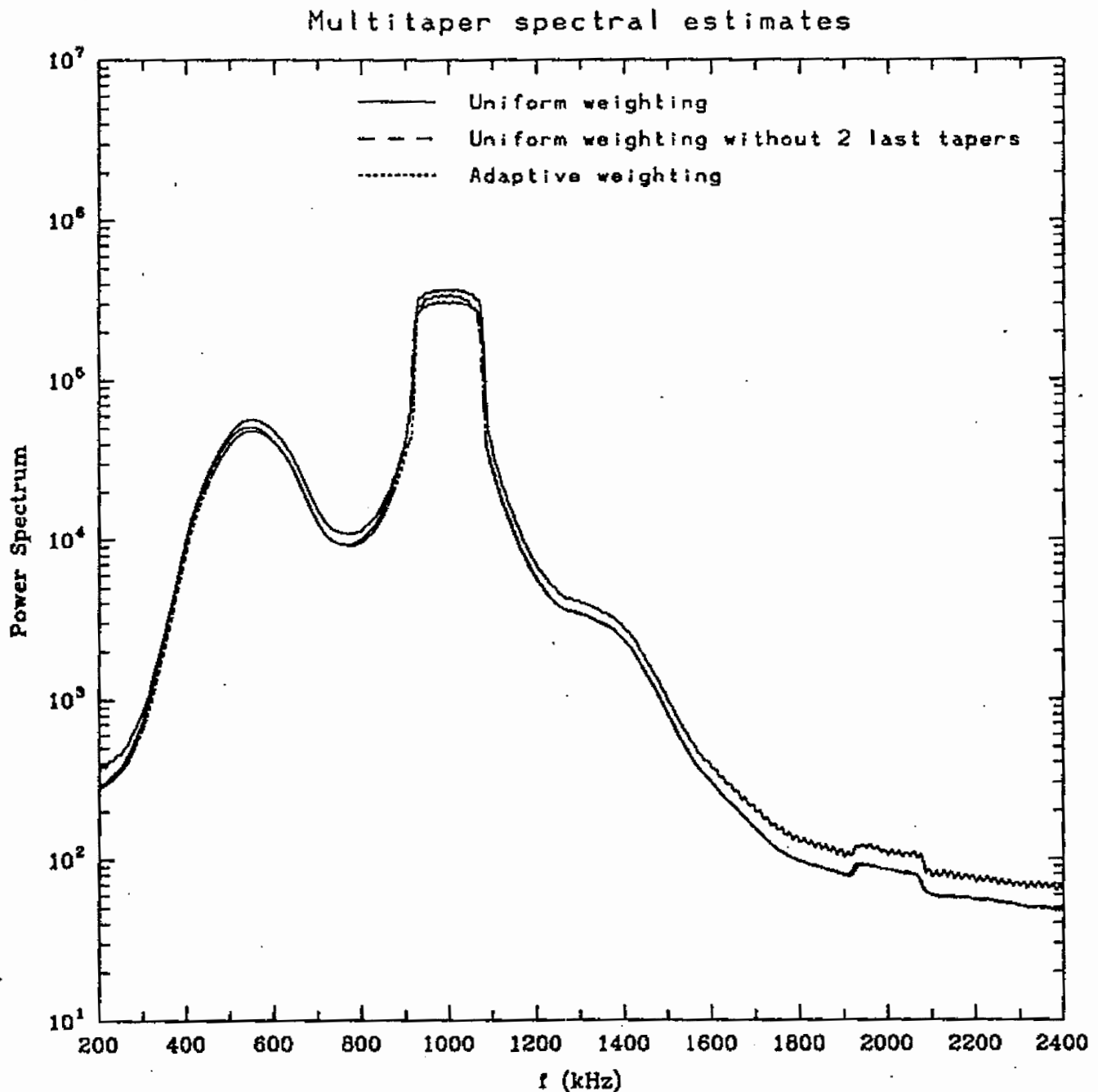


FIG. 9. Multiple taper spectral estimate averaged over 299 overlapping 300 point segments. The adaptive weightings downweight the last several tapers when the inferred broadbanded bias is too large. Solid line: Uniform weighting of $1/(K+1)$. Dashed line: Uniform weighting without the last two tapers. Dotted line: Adaptive multitaper using sequential deselection.

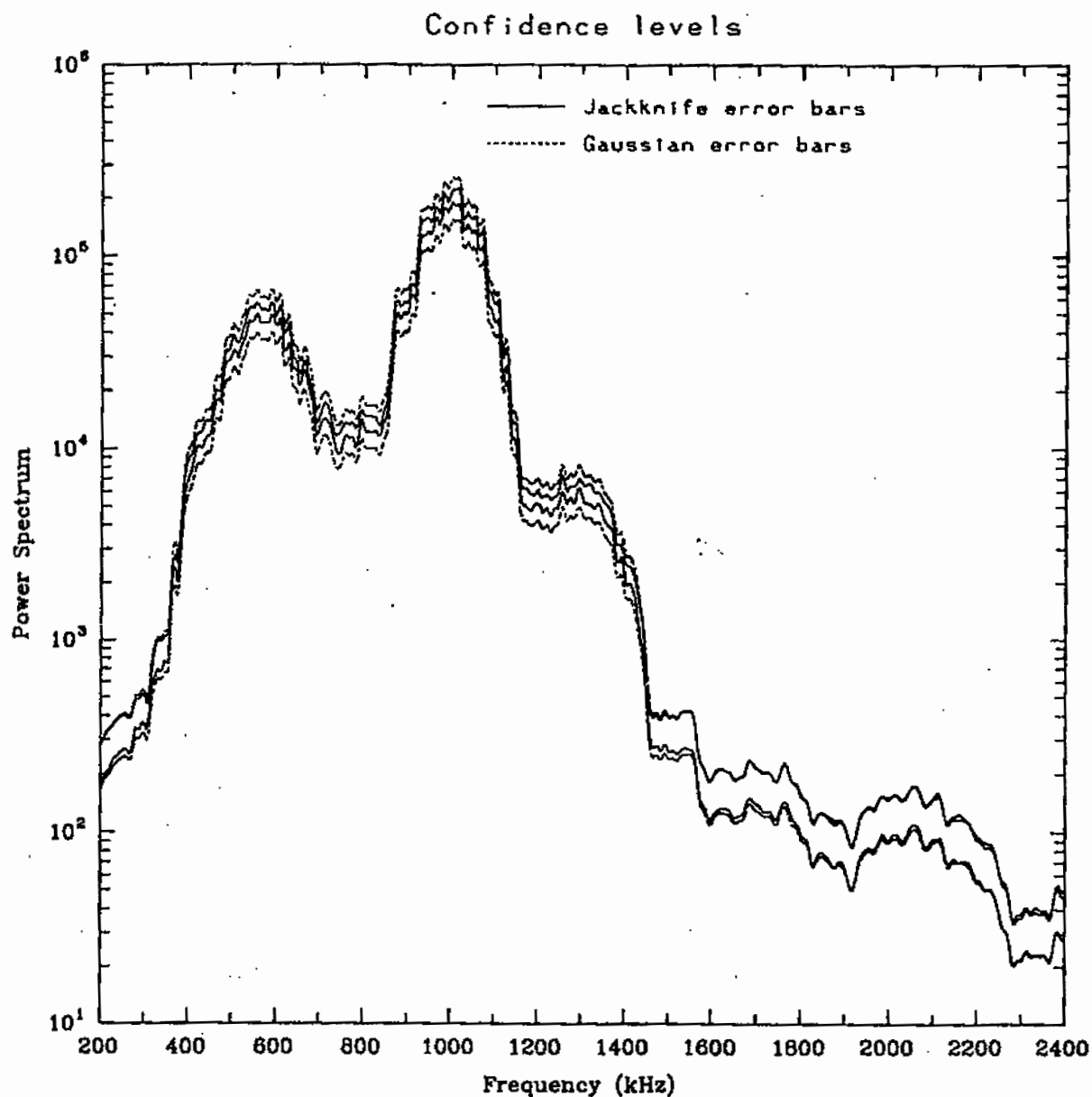


FIG. 10. Resampled versus Gaussian 2σ confidence interval comparison: The jackknife error bars are calculated by resampling the empirical distribution of the individual multitaper estimates, $S^{(k)}(f)$. Thus the jackknife error bars correspond to the actual distribution of the random process. The dotted line gives the error bars for *Gaussian* processes, calculated from the fourth moment identity of Gaussian processes. The Gaussian error bars are actually larger than the empirical error bars near the spectral peaks. This probably occurs because the spectral peaks are partially coherent while Gaussian error bars assumes that there is no coherent component. Solid line: Jackknife error bars for 300 points. Dotted line: Gaussian error bars.

Various taperings for smoothed periodogram

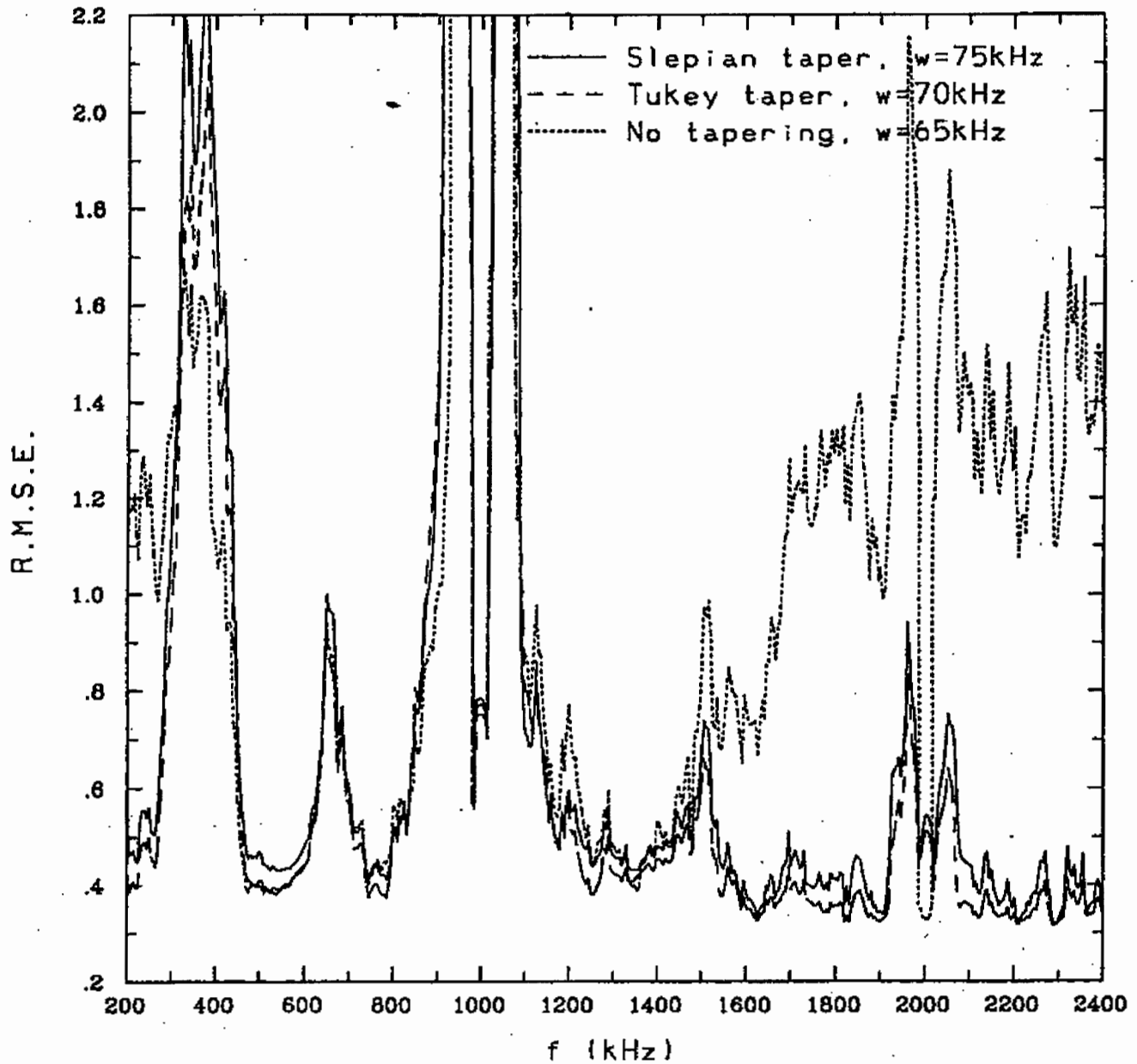


FIG. 11. Normalized RMSE: $\text{RMSE}(f)/S_{\text{Con}}(f)$ of various tapers for the smoothed periodogram, where $\text{RMSE}(f) = |\text{Var}(f) + \hat{B}^2(f)|^{1/2}$. The RMSE is calculated from 299 estimates of 300 point overlapping subsegments. Solid line: Slepian taper, $W=75$ kHz, $\bar{W}=1.0$. Dashed line: Tukey split cosine taper, $W=70$ kHz, $\alpha N=33$. Dotted line: No tapering, $W=65$ kHz.

Adaptive weightings comparison

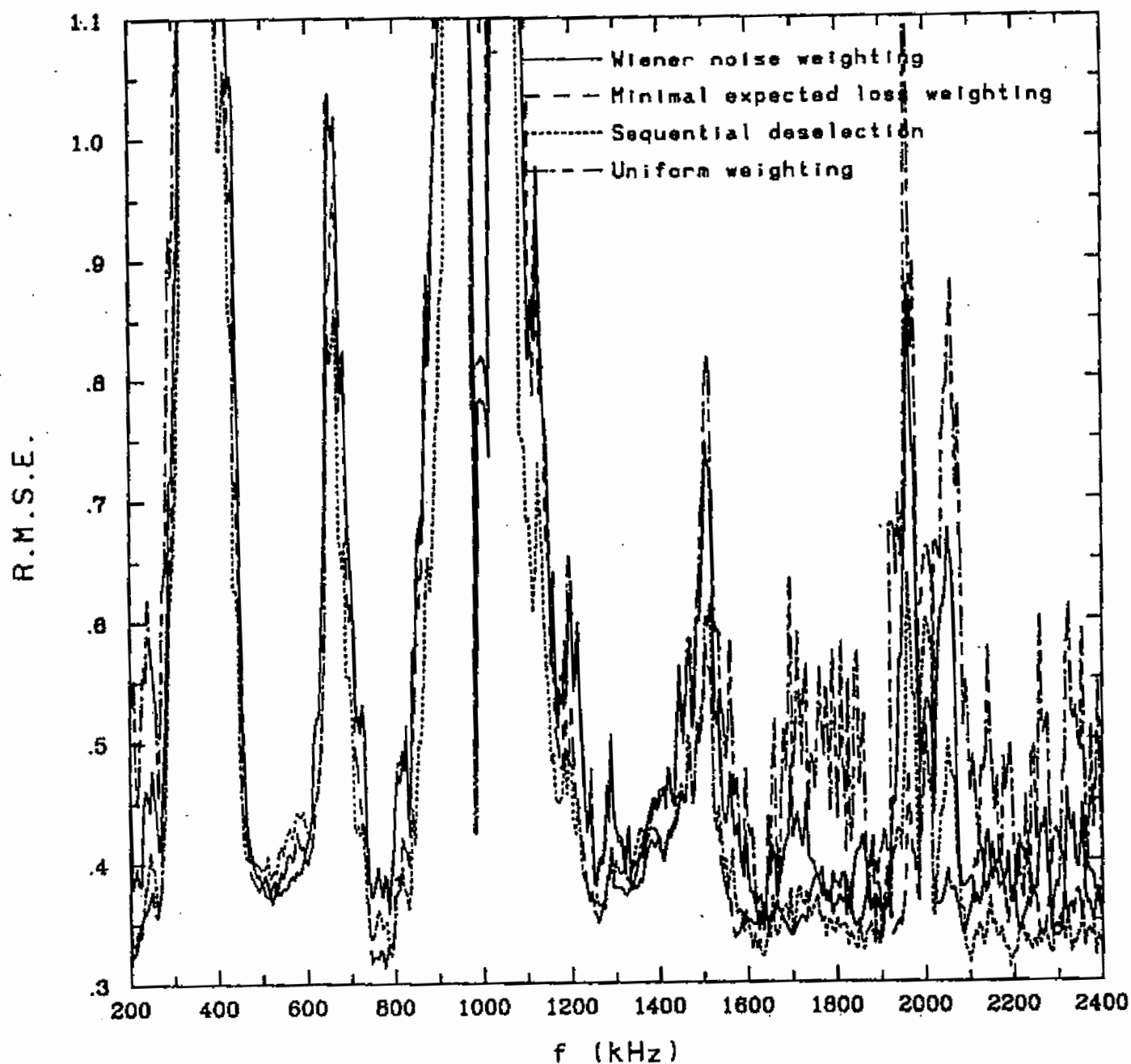


FIG. 12. Normalized RMSE: $RMSE(f)/S_{Con}(f)$ of various adaptive multitaper weightings, where $RMSE(f) = |\hat{Var}(f) + \hat{B}^2(f)|^{1/2}$. Solid

Spectral Estimation Comparison

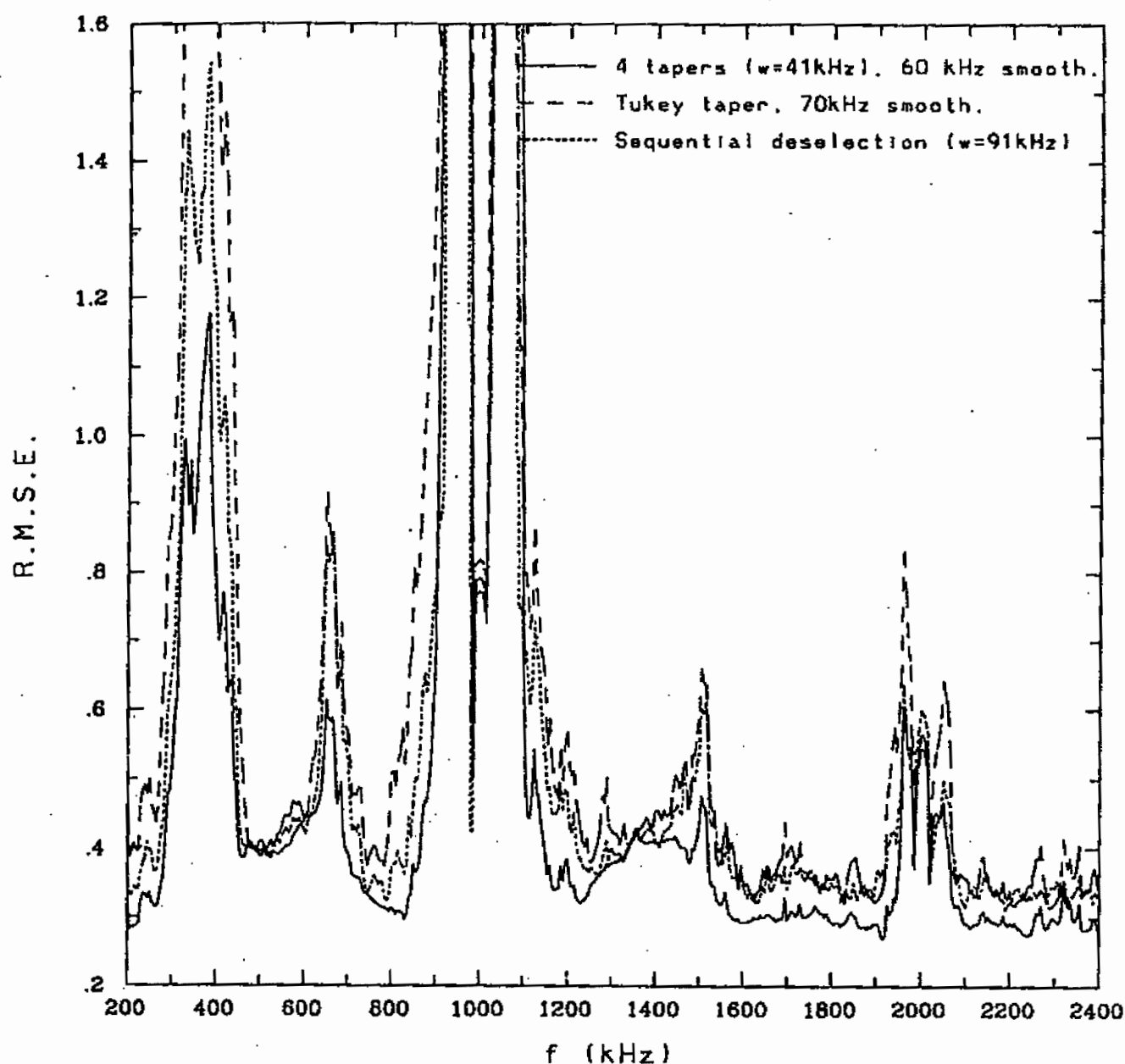


FIG. 13. Normalized RMSE for multitaper-smoothed multitaper-smoothed periodogram comparison. *The smoothed four taper estimate outperforms either "pure" method.* The RMSE is calculated from 150 estimates of 300 point nonoverlapping subsegments. Solid line: Smoothed 4 taper hybrid estimate, $W=60$ kHz, $\bar{W}=2.46$. Dashed line: Smoothed tapered periodogram with $W=70$ kHz using the Tukey split cosine taper with $\alpha N=33$. Dotted line: Adaptive multitaper using sequential deselection $W=91$ kHz.

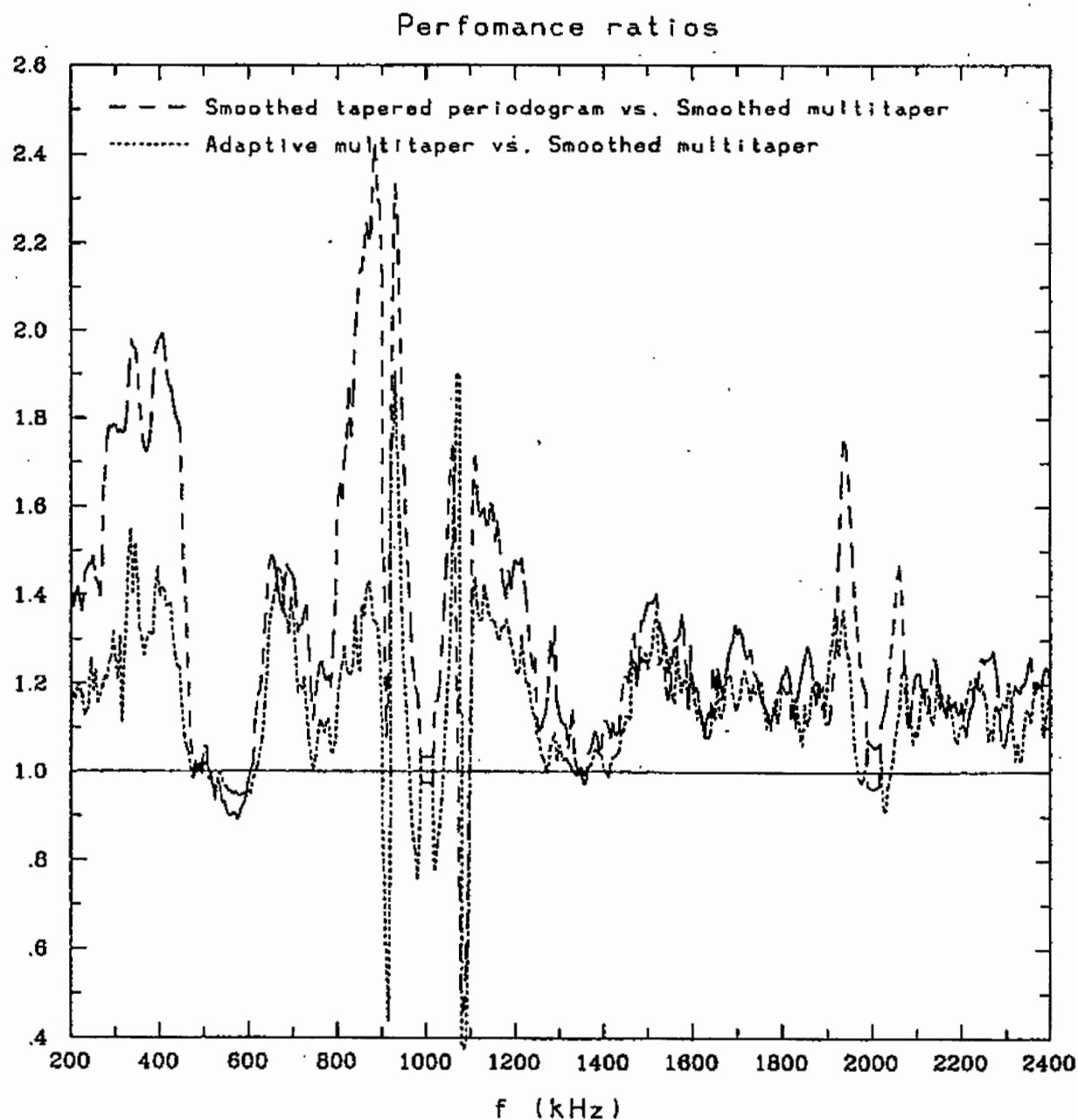


FIG. 14. Performance ratios of multitaper and smoothed tapered periodogram to the smoothed multitaper. Dashed line: RMSE of the smoothed tapered periodogram divided by RMSE of the smoothed multitaper. Dotted line: RMSE of the adaptive multitaper divided by RMSE of the smoothed multitaper.

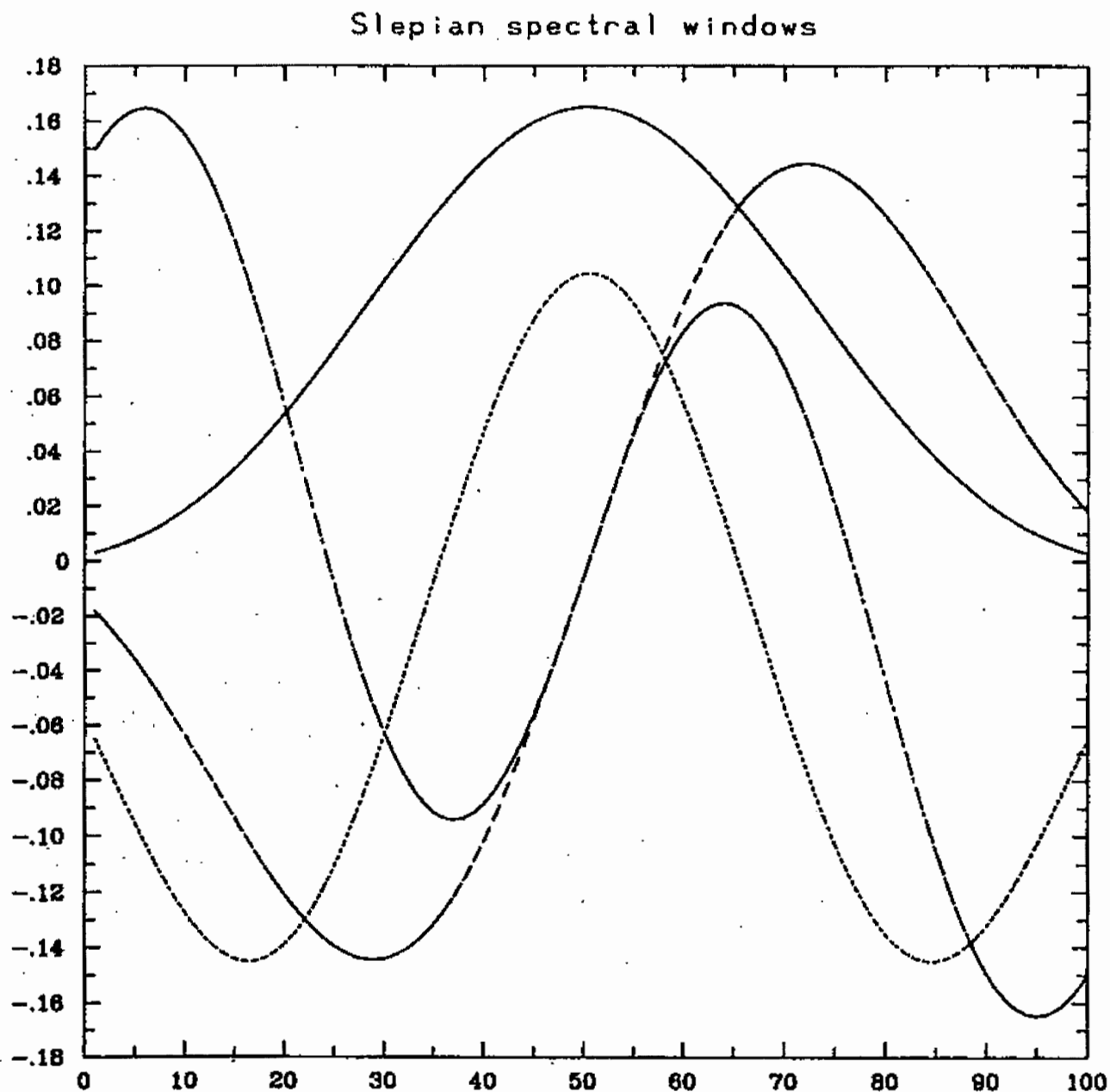


FIG. 15. First four Slepian spectral windows for $N=100$, $W=100$ kHz. The zeroth order taper resembles a standard windowing function. Each successive window has an additional oscillation. Thus the spectral windows resemble Hermite polynomials modulated by a Gaussian.

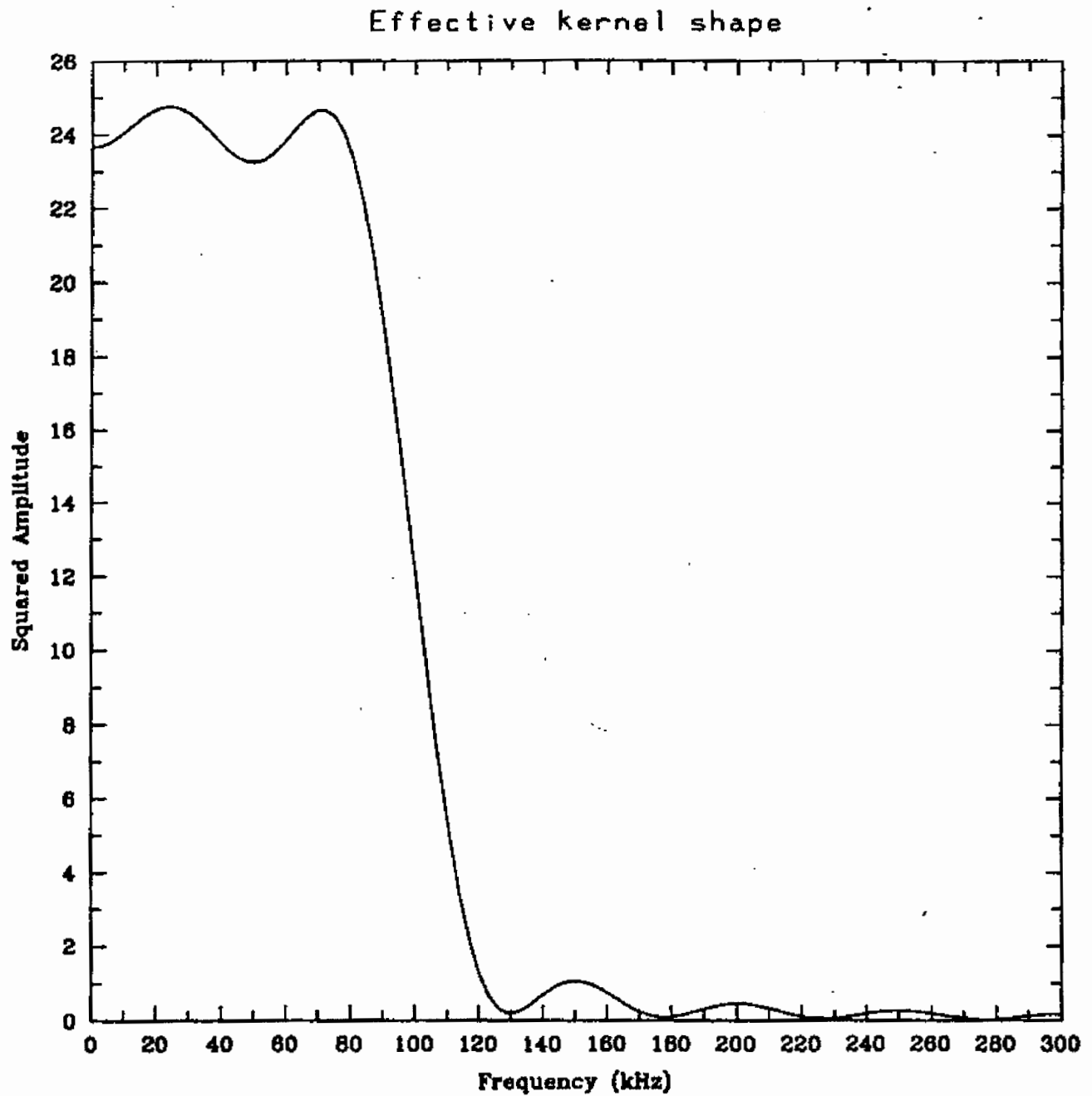


FIG. 16. The effective kernel shape, $\sum_{k=1}^{K=2NW} |V_k(f;N,W)|^2$, versus frequency. As N increases for fixed W , the kernel becomes a step function with bandwidth, W .

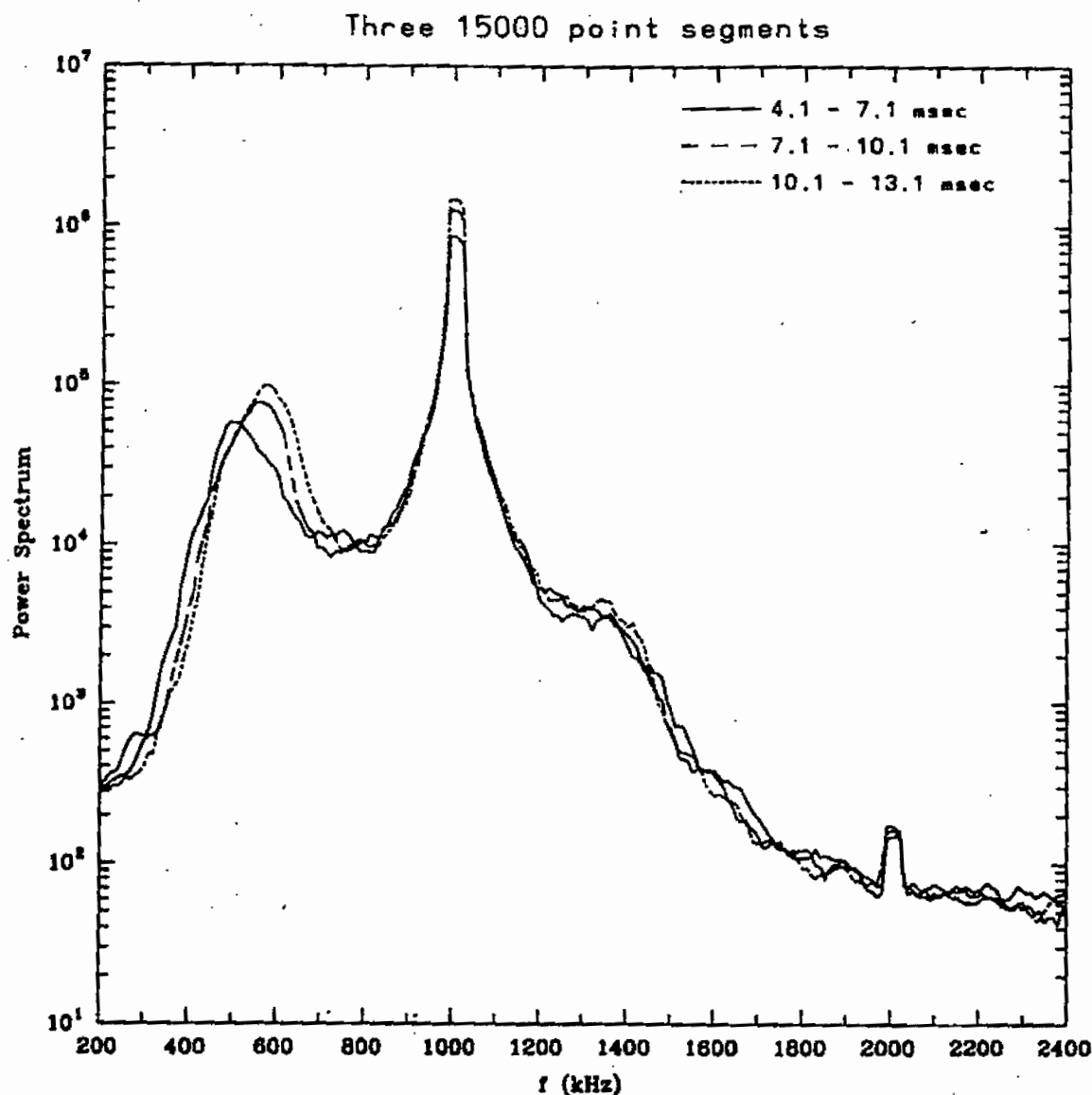


FIG. 17. Adaptive multitaper spectral estimates of three nonoverlapping 15 000 point segments using sequential deselection $W=20$ kHz, 120 tapers. Differences are visible only at the secondary maximum at $550 \text{ kHz} \pm 100 \text{ kHz}$. The secondary maximum represents the electron drift wave fluctuations, which are growing on the ten millisecond time scale. Due to this nonstationarity, our empirical convergence study may not be relevant in the 400–600 kHz frequency range. Solid Line: $t=4.1\text{--}7.1$ ms. Dashed line: $t=7.1\text{--}10.1$ ms. Dotted line: $t=10.1\text{--}13.1$ ms.

Figure Captions:

Figure 1: Comparison of tapered and untapered kernels for $N = 100$: The central lobe of the tapered kernel is broader than the Fejér kernel while the sidelobes are reduced.

Solid line: Fejér kernel, $\frac{1}{N} \left[\frac{\sin(N\pi f)}{\sin(\pi f)} \right]^2$, versus f .

Dashed line: Squared amplitude of Slepian spectral window, $|V(f)|^2$, versus f for $\bar{W} = .6$ ($W = 30$ kHz).

Figure 2: Fejér kernel and squared Slepian spectral window $\bar{W} = .6$ ($W = 10$ kHz), log scale for $N = 300$. Both the tapered and untapered kernels decay as f^{-2} . The amplitude of the tapered sidelobes is reduced proportional to $\exp(-NW)$ relative to the Fejér kernel.

Figure 3: Periodogram of entire 45,000 point segment, log scale. The rapid oscillations occur because the point estimates, $|y(f)|^2$, are nearly uncorrelated at frequencies of $1/N\Delta t$ apart. If the fluctuations were Gaussian and resolved in frequency, the periodogram would have a χ^2_2 distribution.

Figure 4: Spectral estimates of 300 point segment beginning at $t = 8.6$, log scale. The high variance of the unsmoothed periodogram obscurs the systematic differences due to tapering.

Solid line: Periodogram.

Dashed line: Smoothed periodogram with $W = 70$ kHz.

Dotted line: Smoothed tapered periodogram with $W = 70$ kHz using the Tukey split cosine taper with $\alpha N = 33$.

Figure 5: Smoothed spectrum of entire 45,000 point segment, $W = 14$ kHz. The central peak at 1 MHz is partially coherent and is believed to be due to fluctuations at the plasma edge. The secondary peak at 550 kHz is generated by fluctuations which are propagating in the electron drift direction. These fluctuations have a frequency spread of ± 100 kHz.

Solid line: Multitaper estimate with sequential deselection.

Dashed line: Tukey split cosine taper with $\alpha N = 100$.

Dotted line: Periodogram.

Figure 6: Smoothed tapered periodogram for the 300 point subsegment of Fig. 4 for three different kernel halfwidths, 40 kHz, 70 kHz, 120 kHz. As the kernel halfwidth

increases, the spectrum is smoothed and artificially broadened. The area under the 1 MHz peak is approximately conserved.

Solid line: $W = 40$ kHz.

Dashed line: $W = 70$ kHz.

Dotted line: $W = 120$ kHz.

Figure 7: Relative RMSE of the three different kernel halfwidths, averaged over 299 different subsegments. The calculation of the RMSE is described in Appendix D. $W = 40$ kHz does best at the spectral peaks, $W = 120$ kHz does best at the high frequency, and $W = 70$ kHz does best overall.

Solid line: $W = 40$ kHz.

Dashed line: $W = 70$ kHz.

Dotted line: $W = 120$ kHz.

Figure 8: Adaptive multiple taper spectral estimate of 300 point segment beginning at $t = 8.6$. Figs. 6 & 8 are similar, showing that choosing the correct bandwidth is the most important aspect of spectral estimation. For the same “official” bandwidth, the effective bandwidth of the smoothed tapered periodogram is larger than that of the multitaper estimate. This additional broadening is proportional to the Rayleigh resolution. For $N = 300$, the Rayleigh resolution frequency, $\frac{1}{300\Delta t} \simeq 17$ kHz, is a significant fraction of the spectral estimation halfwidth. Thus we use slightly larger bandwidths for the multitaper estimate.

Solid line: $W = 58$ kHz.

Dashed line: $W = 91$ kHz.

Dotted line: $W = 141$ kHz.

Figure 9: Multiple taper spectral estimate averaged over 299 overlapping 300 point segments. The adaptive weightings downweight the last several tapers when the inferred broad-banded bias is too large.

Solid Line: Uniform weighting of $\frac{1}{K+1}$.

Dashed line: Uniform weighting without the last two tapers.

Dotted line: Adaptive multitaper using sequential deselection.

Figure 10: Resampled versus Gaussian 2σ confidence interval comparison: The jackknife error bars are calculated by resampling the empirical distribution of the individual multitaper estimates, $S^{(k)}(f)$. Thus the jackknife error bars correspond to the actual distribution of the random process. The dotted line gives the error

bars for *Gaussian* processes, calculated from the fourth moment identity of Gaussian processes. The Gaussian error bars are actually larger than the empirical error bars near the spectral peaks. This probably occurs because the spectral peaks are partially coherent while Gaussian error bars assumes that there is no coherent component.

Solid line: Jackknife error bars for 300 points.

Dotted line: Gaussian error bars.

Figure 11: Normalized RMSE: $RMSE(f)/S_{Con}(f)$ of various tapers for the smoothed periodogram, where $RMSE(f) = |\widehat{Var}(f) + \hat{B}^2(f)|^{1/2}$. The RMSE is calculated from 299 estimates of 300 point overlapping subsegments.

Solid line: Slepian taper, $W = 75$ kHz, $\bar{W} = 1.0$.

Dashed line: Tukey split cosine taper, $W = 70$ kHz, $\alpha N = 33$.

Dotted line: No tapering, $W = 65$ kHz.

Figure 12: Normalized RMSE: $RMSE(f)/S_{Con}(f)$ of various adaptive multitaper weightings, where $RMSE(f) = |\widehat{Var}(f) + \hat{B}^2(f)|^{1/2}$.

Solid line: Wiener noise adaptive weighting (Eq. B6), $W = 83$ kHz.

Dashed line: Minimal expected loss adaptive weighting (Eq. B5), $W = 91$ kHz.

Dotted line: Adaptive multitaper using sequential deselection, $W = 91$ kHz.

Dashed-Dotted line: Uniform weighting, $W = 83$ kHz.

Figure 13: Normalized RMSE for multitaper – smoothed multitaper – smoothed periodogram comparison. *The smoothed four taper estimate outperforms either “pure” method.* The RMSE is calculated from 150 estimates of 300 point nonoverlapping subsegments.

Solid line: Smoothed 4 taper hybrid estimate, $W = 60$ kHz, $\bar{W} = 2.46$.

Dashed line: Smoothed tapered periodogram with $W = 70$ kHz using the Tukey split cosine taper with $\alpha N = 33$.

Dotted line: Adaptive multitaper using sequential deselection, $W = 91$ kHz.

Figure 14: Performance ratios of multitaper and smoothed tapered periodogram to the smoothed multitaper.

Dashed line: RMSE of the smoothed tapered periodogram divided by RMSE of the smoothed multitaper.

Dotted line: RMSE of the adaptive multitaper divided by RMSE of the smoothed multitaper.

Figure 15: First four Slepian spectral windows for $N = 100$, $W = 100$ kHz.

The zeroth order taper resembles a standard windowing function. Each successive window has an additional oscillation. Thus the spectral windows resemble Hermite polynomials modulated by a Gaussian.

Figure 16: The effective kernel shape, $\sum_{k=1}^{K=2NW} |V_k(f; N, W)|^2$, versus frequency. As N increases for fixed W , the kernel becomes a step function with bandwidth, W .

Figure 17: Adaptive multitaper spectral estimates of three nonoverlapping 15,000 point segments using sequential deselection $W = 20$ kHz, 120 tapers. Differences are visible only at the secondary maximum at $550 \text{ kHz} \pm 100 \text{ kHz}$. The secondary maximum represents the electron drift wave fluctuations, which are growing on the ten millisecond time scale. Due to this nonstationarity, our empirical convergence study may not be relevant in the 400–600 kHz frequency range.

Solid Line: $t = 4.1 - 7.1$ millisecc.

Dashed line: $t = 7.1 - 10.1$ millisecc.

Dotted line: $t = 10.1 - 13.1$ millisecc.